



TÉCNICO
LISBOA

Super-resolution for microwave breast cancer detection

Marco Miguel Valente Gomes

Thesis to obtain the Master of Science Degree in

Electrical and Computer Engineering

Supervisors: Prof. Carlos António Cardoso Fernandes

Prof. João Manuel de Almeida Monteiro Felício

Examination Committee

Chairperson: Prof. José Eduardo Charters Ribeiro da Cunha Sanguino

Supervisor: Prof. Carlos António Cardoso Fernandes

Member of the Committee: Prof. Marco Alexandre dos Santos Ribeiro

November 2023

Declaration

I declare that this document is an original work of my own authorship and that it fulfils all the requirements of the Code of Conduct and Good Practices of the Universidade de Lisboa.

Acknowledgements

I would like to thank Professor Carlos Fernandes for the challenge proposed in this thesis, for all the feedback provided during its development, with comments and suggestions that piqued my interest and encouraged me to explore further. To Professor João Felício, thank you for all the time and patience you dedicated to helping me understand complex concepts and for the continuous support in the laboratory. Thanks to Raquel Martins for the availability to assist in in the setups and for the creative ideas provided to facilitate the work. A big thank you to Professor David Fernandes and Professor Sérgio Matos for all the suggestions and constructive criticism provided during meetings, which helped me gain a better understanding of the concepts and made the work more comprehensible.

I would also like to thank Instituto de Telecomunicações for providing all the infrastructure necessary to carry out the thesis, this work was funded by Fundação para a Ciência e Tecnologia (FCT/MCTES) and co-funded by FEDER-PT2020 partnership agreement under projects UIDB/50008/2020 and 2022.04764.PTDC (IRMIS).

Finally, I would like to express my gratitude to my family and friends, whose unwavering support and encouragement helped me complete this work.

Abstract

The development of super-resolution microwave imaging techniques has led to significant advancements in breast cancer diagnosis, a crucial field of medical diagnostics. This thesis explores the assessment and use of high-permittivity materials as lenses to improve the resolution of microwave imaging for the diagnosis of breast cancer, particularly agar and ultrasound gel.

The research involves a comprehensive exploration of these high-permittivity materials. Through the assessment of their impact on image reconstruction and detection capabilities via numerical simulations and experimental testing, this study reveals promising outcomes in certain conditions. It highlights the efficacy of these materials in enhancing imaging resolution.

Additionally, the study uncovers the limitations linked to high-permittivity materials in specific scenarios, providing insights into the intricate relationship between lens properties and their impacts on imaging capabilities. This highlights the intricate challenges and opportunities in optimizing breast cancer diagnostic technologies.

Overall, this thesis explores the technologies and algorithms used in super-resolution microwave imaging for breast cancer detection. It provides insights into its potential, limitations, and the prospects for advancing diagnostic technologies.

Keywords

Anisotropic refractive index, Dielectric Slab, High-Permittivity materials; Microwave Imaging; Super-resolution

Resumo

O desenvolvimento de técnicas de imagem de micro-ondas de super resolução tem levado a avanços significativos no diagnóstico do cancro da mama, um campo crucial na área da medicina. Esta tese explora a avaliação e utilização de materiais de alta permitividade como lentes para melhorar a resolução da imagem de micro-ondas no diagnóstico do cancro da mama, em particular o agar e o gel de ultrassom.

A investigação envolve uma exploração abrangente destes materiais de alta permitividade. Através da avaliação do seu impacto na reconstrução de imagens e capacidades de deteção por meio de simulações numéricas e testes experimentais, este estudo revela resultados promissores em certas condições. Destaca a eficácia destes materiais na melhoria da resolução da imagem.

Além disso, o estudo desvenda as limitações associadas aos materiais de alta permitividade em cenários específicos, fornecendo informações sobre a relação complexa entre as propriedades da lente e os seus impactos nas capacidades de imagem. Isto realça os desafios complexos e as oportunidades na otimização das tecnologias de diagnóstico do cancro da mama.

Resumindo, esta tese explora as tecnologias e algoritmos utilizados na imagem de micro-ondas de super resolução para o diagnóstico do cancro da mama. Fornece perspetivas sobre o seu potencial, limitações e as perspetivas para o avanço das tecnologias de diagnóstico.

Palavras-chave

Índice de Refração Anisotrópico; Placa Dielétrica; Materiais de Elevada Permitividade; Imagem por Micro-ondas; Super-resolução;

Index

1	Introduction.....	1
1.1	Motivation and objectives	2
1.2	Work highlights	2
2	Fundamental concepts.....	3
2.1	Propagation in dielectric slab lenses	4
2.1.1	Symmetric dielectric slab.....	4
2.1.2	Asymmetrical dielectric slab	6
2.2	Image reconstruction	10
2.3	Image quality metrics.....	12
3	State of the art.....	15
3.1	Microwave imaging for breast cancer.....	16
3.2	Super-resolution Imaging	19
4	Numerical and Simulation Results	21
4.1	Super-resolution validation and imaging	22
4.2	Super Lenses Simulation inside breast.....	26
4.2.1	Lens Attenuation.....	26
4.2.2	Super-resolution Detection Simulation	30
5	Experimental Results	41
5.1	Detection with symmetrical slab	42
5.2	Detection with asymmetrical slab	47
6	Conclusions.....	57
6.1	Main achievements.....	58
6.2	Future Work.....	59
	Bibliography.....	60

List of figures

Figure 2.1. Schematic of dielectric slab (extracted from [9])	4
Figure 2.2. Graphical resolution of the system of equations	5
Figure 2.3 Attenuation as a function of slab thickness for a frequency of 5 GHz.	7
Figure 2.4 Attenuation as a function of slab thickness for a frequency of 10 GHz.	8
Figure 2.5 Attenuation as a function of frequency for a slab thickness of 1 mm.	8
Figure 2.6 Attenuation as a function of frequency for a slab thickness of 0.5 mm.	8
Figure 2.7. Attenuation as a function of k_0d	9
Figure 2.8. Description of the image reconstruction algorithm	11
Figure 2.9. Geometry for the tangential refractive index algorithm	12
Figure 3.1: Monostatic system	16
Figure 3.2: Multistatic system	17
Figure 3.3. BAVA Antenna (extracted from [15])	17
Figure 3.4. XETS Antenna (extracted from [15])	18
Figure 3.5. Reconstructed image for 3mm tumor (extracted from [7])	18
Figure 3.6. Reconstructed image for 5mm tumor (extracted from [7])	18
Figure 3.7. Reflection coefficient in function of position (extracted from [27])	20
Figure 4.1. Geometry of the simulations for super resolution validation	22
Figure 4.2. Super Resolution with water lens and dipole	23
Figure 4.3. Setup for the nx calculation	24
Figure 4.4. Target response in function of the electric distance	24
Figure 4.5. Obtained image with the algorithm, with lens	25
Figure 4.6. Obtained image with the algorithm, in free space	25
Figure 4.7. Setup of the attenuation simulation (perspective view)	26
Figure 4.8. Setup of the attenuation simulation (front view)	26
Figure 4.9. Attenuation for a lens with thickness = 1 mm and permittivity = 78	27
Figure 4.10. Attenuation for a lens with thickness = 0.5 mm and permittivity = 78	27
Figure 4.11. Attenuation for a lens with thickness = 1 mm and permittivity = 60	28
Figure 4.12. Attenuation for a lens with thickness = 0.5 mm and permittivity = 60	28

Figure 4.13. Setup for propagation validation	29
Figure 4.14. Propagation inside the slab at 500 MHz	29
Figure 4.15. Propagation inside the slab at 5 GHz	29
Figure 4.16. Detection Simulation Setup.....	30
Figure 4.17. Variation of n_x with frequency for slab thickness of 1 mm.....	31
Figure 4.18. 1D Image for $z=0$ and slab thickness of 1 mm.....	31
Figure 4.19. 2D Image for depth = 0mm and slab thickness of 1 mm	32
Figure 4.20. 2D Image for depth = 1mm and slab thickness of 1 mm	32
Figure 4.21. 2D Image for depth = 2 mm and slab thickness of 1 mm	33
Figure 4.22. 2D Image for depth = 3 mm and slab thickness of 1 mm	33
Figure 4.23. Variation of n_x with frequency for slab thickness of 0.5 mm.....	34
Figure 4.24. 1D Image for $z = 0$ and slab thickness of 0.5 mm.....	34
Figure 4.25. 2D Image for depth = 0 mm and slab thickness of 0.5 mm	35
Figure 4.26. 2D Image for depth = 1 mm and slab thickness of 0.5 mm	36
Figure 4.27. 2D Image for depth = 2 mm and slab thickness of 0.5 mm	36
Figure 4.28. 2D Image for depth = 3 mm and slab thickness of 0.5 mm	37
Figure 4.29. Setup for cylindrical breast.....	37
Figure 4.30. Variation of n_x with frequency for slab thickness of 1mm and cylindrical breast ...	38
Figure 4.31. 2D Image for detection with no lens.....	38
Figure 4.32. 2D Image for detection with lens for a depth of 0 mm	39
Figure 4.33. 2D Image for detection with lens for a depth of 1 mm	39
Figure 5.1. Permittivity vs frequency for Agar, Aloe vera Gel and Ultrasound Gel	42
Figure 5.2. Conductivity vs frequency for Agar, Aloe vera Gel and Ultrasound Gel	42
Figure 5.3. Permittivity and $\tan\delta$ of water	43
Figure 5.4. Experimental setup (without lens) for symmetrical slab.....	44
Figure 5.5. Experimental setup (with lens) for symmetrical slab.....	44
Figure 5.6. Image without lens with $\text{distTargets} = 14$ mm.....	45
Figure 5.7. 1D Image for Agar Lens with $\text{distTargets} = 14$ mm	45
Figure 5.8. 1D Image for Agar Lens with $\text{distTargets} = 9$ mm	45
Figure 5.9. 1D Image for Agar Lens with $\text{distTargets} = 5.5$ mm	46

Figure 5.10. 1D Image for Ultrasound Gel Lens with distTargets = 14 mm	46
Figure 5.11. 1D Image for Ultrasound Gel Lens with distTargets = 5.5 mm	47
Figure 5.12. Setup for Radial measurements	48
Figure 5.13. Front view for radial setup with lens and distTargets = 30 mm	48
Figure 5.14. Front view for radial setup with lens and distTargets = 20 mm	49
Figure 5.15. Front view for radial setup with lens and distTargets = 10 mm	49
Figure 5.16. Front view for radial setup without lens and distTargets = 24 mm	49
Figure 5.17. Front view for radial setup without lens and distTargets = 14 mm	50
Figure 5.18. Front view for radial setup without lens and distTargets = 4 mm	50
Figure 5.19. Reconstructed image for setup with no lens, with distTarget = 24 mm	51
Figure 5.20. Reconstructed image for setup with no lens, with distTarget = 14 mm	51
Figure 5.21. Reconstructed image for setup with no lens, with distTarget = 4 mm	51
Figure 5.22. Variation of n_x with frequency for slab thickness of 1 mm and cylindrical breast, for the experimental setup	52
Figure 5.23. Reconstructed image for setup with lens, with distTargets = 24 mm, depth = 0 mm	52
Figure 5.24. Reconstructed image for setup with lens, with distTargets = 24 mm, depth = 7 mm	53
Figure 5.25. Reconstructed image for setup with lens, with distTargets = 24 mm, depth = 14 mm	53
Figure 5.26. Reconstructed image for setup with lens, with distTargets = 14 mm, depth = 0 mm	53
Figure 5.27. Reconstructed image for setup with lens, with distTargets = 14 mm, depth = 7 mm	54
Figure 5.28. Reconstructed image for setup with lens, with distTargets = 14 mm, depth = 14 mm	54
Figure 5.29. Reconstructed image for setup with lens, with distTarget = 4 mm, depth = 0 mm	54

List of tables

Table 4.1. Bandwidth of monomodal propagation.....	28
--	----

List of Acronyms

BAVA	Balanced antipodal Vivaldi antenna.
CD	Compact Disk
CST	Computer Simulation Technology
MATLAB	Matrix Laboratory
PE	Positioning Error
PEC	Perfect Electric Conductor
PLA	Polylactic acid
RMS	Root Mean Square
TCR	Tumor-to-clutter Ratio
TE	Transverse Electric
TM	Transverse Magnetic
TMR	Tumor-to-mean Ratio
TPU	Thermoplastic Polyurethane
TX-100	Triton X-100
VNA	Vector Network Analyzer
XETS	Crossed Exponentially Tapered Slot

List of Symbols

λ	Wavelength
μ	Permeability
β	Propagation constant
α	Attenuation constant
ω	Angular frequency
ε	Permittivity
f	Frequency
n	Refractive index
k_0	Free space propagation constant
Γ	Reflection coefficient
x, y	Cartesian coordinates
ρ, ϕ	Polar coordinates

1 Introduction

The introduction chapter aims to provide a brief overview of the research topic and its significance. The problem of breast cancer detection and the current limitations of existing imaging techniques will be discussed, highlighting the need for more effective and accurate methods. The focus of this work will be on microwave imaging systems, and their potential for breast cancer detection using super resolution techniques. The chapter will also outline the research objectives and the highlights of the work.

1.1 Motivation and objectives

Nowadays, breast cancer is the most prevalent form of cancer worldwide [1]. One of the ways to increase the survival rate of the patients is by getting an early diagnosis of the disease, however the current diagnostic tools are limited. The techniques currently used for breast cancer detection, such as X-rays[2], [3], magnetic resonance imaging[4], and PET scans[5], possess numerous disadvantages including the use of ionizing radiation, high costs, and invasiveness. It is crucial to find a solution that minimizes these downsides while achieving the detection of similar tumors.

There are studies related to the use of microwave imaging to detect breast cancer [6]–[8]. This method uses radar techniques to detect the dielectric contrast between tumors and healthy breast tissue, yet the resolution of the images obtained by this method is not very high, because these systems are limited by Rayleigh's diffraction limit and can lead to false diagnosis.

The main advantages of using microwave imaging to detect breast cancer are the comfort of the patient, the non-ionizing radiation that is safe to the user and the low cost.

The two main difficulties of using microwave imaging to detect breast cancer are the reflection of the skin of the breast which is much greater than the tumor reflection response, and the necessary wavelength for electromagnetic energy to penetrate the breast that hinders the obtainment of good resolutions.

The objective of this work is to use super-resolution techniques, to increase the image definition and resolution of microwave imaging in early breast cancer detection (in superficial tumors), and to decrease the reflection losses by the breast skin.

1.2 Work highlights

The current systems are physically constrained, unable to achieve resolutions lower than $\lambda/2$ due to the Rayleigh diffraction limit (as it will be explained in Chapter 2). Consequently, it is imperative to investigate mechanisms that can enhance this resolution. Super lenses, represented by dielectric slabs, accomplish this super-resolution, necessitating a comprehensive study of the propagation mechanisms within these slabs.

Subsequently, the implementation of this dielectric slab into the existing breast cancer detection setup at the Instituto de Telecomunicações is required. This entails researching and testing materials suitable for constructing this superlens.

Finally, the effectiveness of this superlens in detecting tumors with greater resolution (primarily superficial tumors) needs to be rigorously tested within the setup. This sequential process aims to contribute to advancing microwave breast cancer detection technology, with a particular focus on achieving enhanced resolution through the application of superlenses.

2 Fundamental concepts

In this chapter fundamental concepts related to propagation on dielectric slab lenses are introduced to support the basis of super resolution for the detection of the small superficial tumors, the equations of all the propagation modes and how to solve them and the condition to have single mode propagation is described. The image reconstruction algorithm utilized to create 2D images of the breast with the detected tumors is explained and the image quality metrics found in the state of the art are presented.

2.1 Propagation in dielectric slab lenses

A dielectric slab supports a slow surface wave, the higher the refractive index is, the slower this surface wave will propagate. This causes the field around the slab to be evanescent (instead of propagating), preserving resolution and surpassing the limit of $\lambda/2$ associated with propagation (Rayleigh's diffraction limit).

The propagation of electromagnetic waves in dielectric slabs occurs similarly to what happens in waveguides, there are two media with different refractive indices (where the refractive index of the slab must be higher than the refractive index of the medium covering it), there are two types of modes of propagation TE (transverse electric) and TM (transverse magnetic). In the TE modes there is only a magnetic field along the direction of propagation and no electric field, in TM modes the opposite occurs, that is, there is an electric field along the direction of propagation and no magnetic field.

The geometry of a dielectric slab is represented in the figure below:

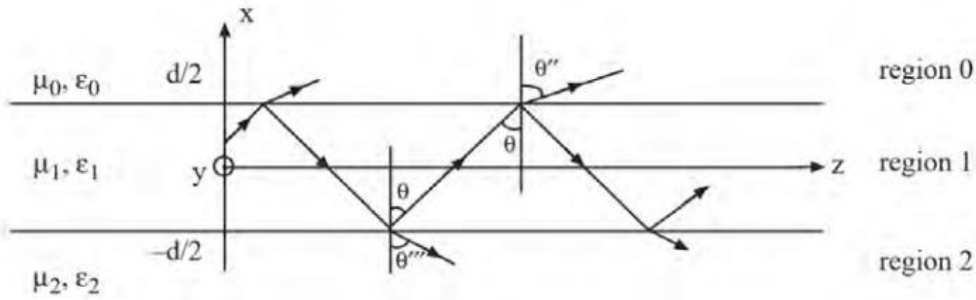


Figure 2.1. Schematic of dielectric slab (extracted from [9])

Where region 1 indicates the slab with a permittivity (ϵ_1) and permeability (μ_1), region 2 has the same properties of region 0 ($\epsilon_2 = \epsilon_0$, $\mu_2 = \mu_0$), and d is the thickness of the slab.

2.1.1 Symmetric dielectric slab

There can be multiple TE_n modes propagating in the slab, the equations that describe the behavior of these modes are the following (2.1 for n even and 2.2 for n odd):

$$\frac{\mu_0 \beta_{1x} d}{\mu_1} \tan\left(\frac{\beta_{1x} d}{2}\right) = \frac{\alpha_{0x} d}{2} \quad (2.1)$$

$$-\frac{\mu_0 \beta_{1x} d}{\mu_1} \cot\left(\frac{\beta_{1x} d}{2}\right) = \frac{\alpha_{0x} d}{2} \quad (2.2)$$

Where μ_0 and μ_1 are the permeability of the region 0 and 1 respectively, β_{1x} is the transverse propagation constant, α_{0x} is the attenuation constant in region 0 (which is equal to region 2 in this case) and d is the thickness of the slab.

An interesting property of these types of slabs is the existence of evanescent waves.

Evanescent waves are formed whenever there is total internal reflection of the waves inside the slab, these waves are not limited by Rayleigh's diffraction limit of $\lambda/2$ so they can be used to increase the resolution of microwave imaging systems [10].

To avoid intermodal interference, it is necessary to have single mode propagation. To achieve this in the dielectric slab it is necessary that only one TE mode is propagating. A simple way of calculating the frequency and thickness necessary so that the slab is in single mode propagation is by solving the equations 2.1 and 2.2 and verifying that there is only one solution to the system of equations, this can also be done graphically by intersecting the two curves and obtaining a point, an example of this is depicted in the following figure:

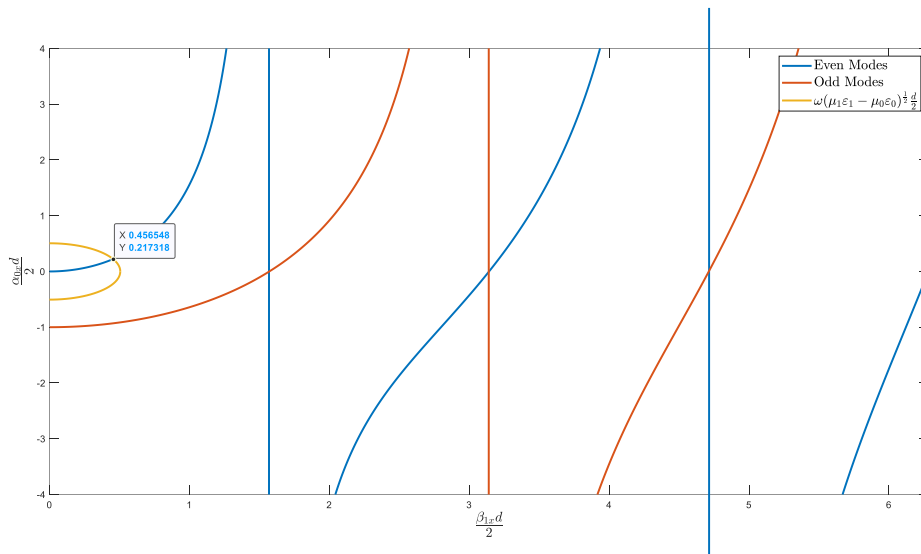


Figure 2.2. Graphical resolution of the system of equations

As shown in Figure 2.2 there is one solution to the system, so the slab is propagating one mode (TE₀), the radius of the circumference is given by:

$$\omega \sqrt{(\mu_1 \epsilon_1 - \mu_0 \epsilon_0)} \times \frac{d}{2} \quad (2.3)$$

Where ω is the angular frequency calculated as $\omega = 2\pi f$.

To decrease the radius of the circumference so that there is only one mode propagating in the slab it is needed to:

- Decrease the frequency of the electromagnetic wave propagating in the slab so that ω decreases.
- Decrease the thickness of the slab.
- Change the material so that $\mu_1 \epsilon_1$ is lower.

As shown in the Figure 2.2, the radius of the circumference in order to have only one mode of propagation (TE₀) must be lower than $\frac{\mu_0}{\mu_1}$, so, it is possible to derive an inequality that allows the calculation of the thickness of the slab in function of this parameters (Equation 2.4).

$$\omega\sqrt{(\mu_1\varepsilon_1 - \mu_0\varepsilon_0)} \times \frac{d}{2} < \frac{\mu_0}{\mu_1} \quad (2.4)$$

2.1.2 Asymmetrical dielectric slab

In contrast to symmetric dielectric slabs, in asymmetric plates, region 0 has electromagnetic characteristics that are different from those of region 2. Given the discrepancy between air and breast tissue in the identification of breast cancer, it is important to study the behavior of these slabs.

The equations for single-mode propagation will differ from those of the symmetric slab, as ε_0 is distinct from ε_2 . The equations for the TE and TM modes, respectively, are as follows: [11]

$$\tan(d\beta_{1x}) = \frac{\alpha_{0x} + \alpha_{2x}}{\beta_{1x} \left(1 - \frac{\alpha_{0x}\alpha_{1x}}{\beta_{1x}^2}\right)} \quad (2.5)$$

$$\tan(d\beta_{1x}) = \frac{\beta_{1x} \left(\frac{n_1^2}{n_2^2}\alpha_{2x} + \frac{n_1^2}{n_0^2}\alpha_{2x}\right)}{\beta_{1x}^2 - \frac{n_1^4}{n_0^2 n_2^2}\alpha_{0x}\alpha_{2x}} \quad (2.6)$$

Where:

$\alpha_{0x}, \alpha_{1x}, \alpha_{2x}$ are the attenuation constants for regions 0, 1 and 2 respectively, β_{1x} is the transverse propagation constant, n_0, n_1, n_2 are the refractive indexes for regions 0, 1 and 2 respectively and d is the thickness of the dielectric slab.

Just like in symmetric dielectric slabs, it is necessary for only one mode to propagate to avoid intermodal interference for algorithm execution. Considering that $n_1 > n_2 > n_0$, the cutoff condition is given by $\beta = k_0 n_2$. It is then possible, using equations 2.5 and 2.6, to derive equations 2.7 and 2.8, providing the number of modes of propagation inside a dielectric slab, for modes TE and TM, respectively:[12]

$$M = \left\{ \frac{1}{\pi} (2v - \tan^{-1} \left[\left(\frac{n_2^2 - n_0^2}{n_1^2 - n_2^2} \right)^{\frac{1}{2}} \right]) \right\}_{int} \quad (2.7)$$

$$M = \left\{ \frac{1}{\pi} (2v - \tan^{-1} \left[\left(\frac{n_1}{n_0} \right)^2 \left(\frac{n_2^2 - n_0^2}{n_1^2 - n_2^2} \right)^{\frac{1}{2}} \right]) \right\}_{int} \quad (2.8)$$

Where:

v is the normalized frequency given by $k_0 d (n_1^2 - n_2^2)^{\frac{1}{2}}$, n_1 and n_2 are the refractive indexes of region 1 and 2.

The attenuation constants are dependent on the refractive index of its region and the longitudinal propagation constant, so it is possible to write the equations so that there is only one variable (β_{1x}).

$$\beta = \sqrt{k_0^2 n_1^2 - \beta_{1x}^2} \quad (2.9)$$

$$\alpha_{0x} = \sqrt{\beta^2 - k_0^2 n_0^2} \quad (2.10)$$

$$\alpha_{2x} = \sqrt{\beta^2 - k_0^2 n_2^2} \quad (2.11)$$

With this information, it is possible to calculate attenuation within any region and plot it in terms of frequency and slab thickness. In the context of breast cancer detection, the region where it is of interest to know the attenuation will be region 2 (breast tissue with ϵ_2 approximately equal to 4). Graphs were then constructed to compare attenuation with region 2 having a permittivity of 4 and with a permittivity of 1 (symmetric case) for various frequencies and slab thicknesses.

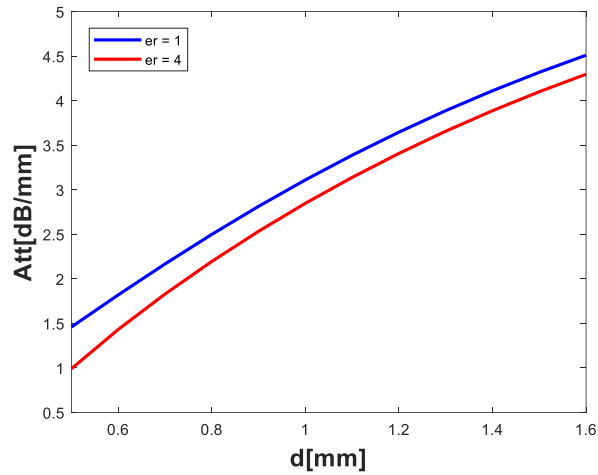


Figure 2.3 Attenuation as a function of slab thickness for a frequency of 5 GHz.

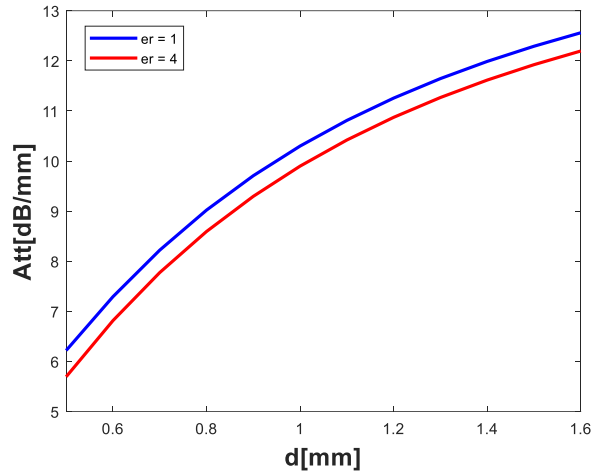


Figure 2.4 Attenuation as a function of slab thickness for a frequency of 10 GHz.

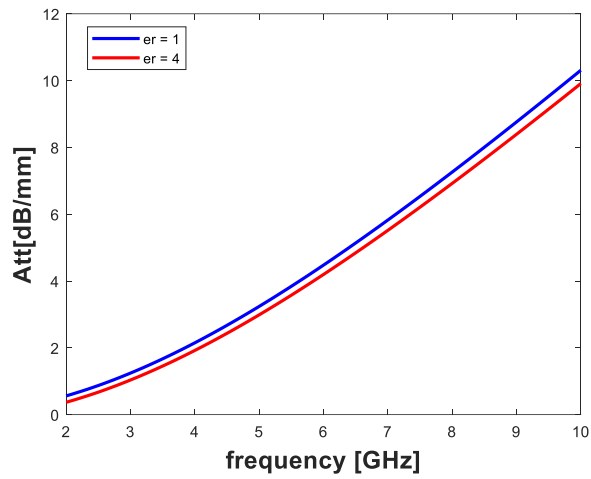


Figure 2.5 Attenuation as a function of frequency for a slab thickness of 1 mm.

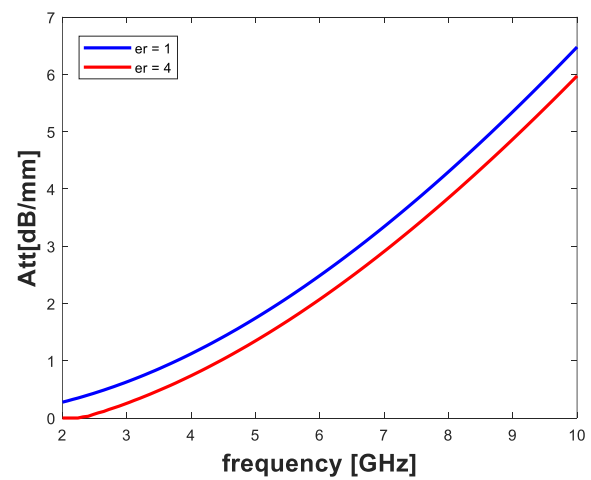


Figure 2.6 Attenuation as a function of frequency for a slab thickness of 0.5 mm.

As can be observed in the figures above, attenuation will increase with both frequency and slab thickness. Hence, it is relevant to manipulate these two parameters to achieve optimal resolution in detection. Frequencies of 5 and 10 GHz were studied, as they are commonly utilized in breast cancer detection. Thicknesses of 0.5 and 1 mm were analyzed because they allow for the propagation of only one mode for the previously mentioned frequencies, as seen in the results of the equations 2.10 and 2.11.

It can further be concluded that with the increase in permittivity of region 2 (from 1 to 4), attenuation decreases. This observation is particularly relevant to the studied application, as it results in lower attenuation within the breast compared to free space, assuming the breast has negligible losses.

It is also possible to plot a graph of the attenuation as a function of k_0d , simultaneously varying the frequency and the thickness of the slab. This allows for the observation of the attenuation behavior with respect to these two parameters, as depicted in the figure below:

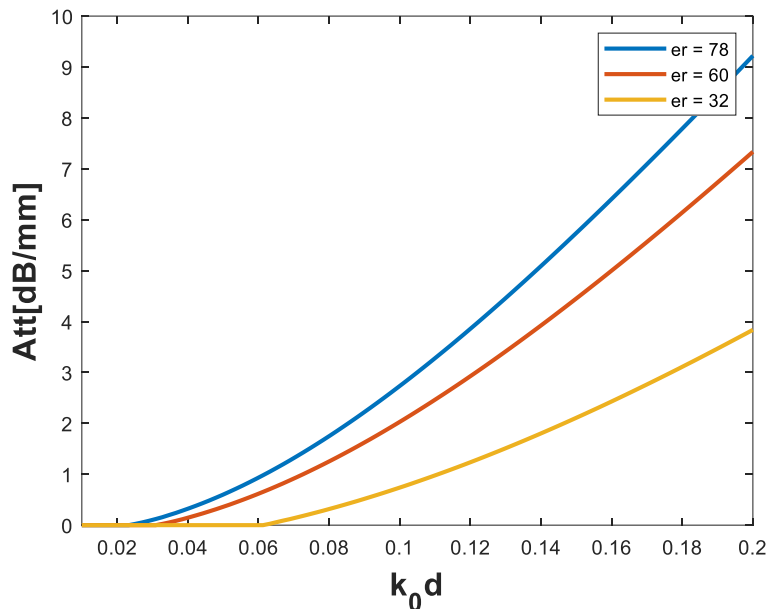


Figure 2.7. Attenuation as a function of k_0d

For this figure, three different permittivity of the dielectric slab were tested (78, 60, and 32 represented in blue, red, and yellow respectively). An increase in attenuation with the permittivity of the slab was observed. Values where the attenuation is equal to 0 should be disregarded, as they are outside the bandwidth where only one mode propagates, meaning frequencies where no mode is propagated in the slab.

2.2 Image reconstruction

It is possible to create an image to represent the detected tumors in the breast through an algorithm based on Kirchhoff Migration, which is a method that is used in geophysics to produce images related to seismic waves [13].

The algorithm used has previously been employed at the Instituto de Telecomunicações, resulting in positive outcomes for microwave imaging for biomedical applications [14] .

This algorithm consists of defining a region of interest where the image will be reconstructed, obtaining the reflection coefficients of various antennas in different positions and for each of these positions calculate the distance of every antenna to all the positions of the region of interest, multiply the reflection coefficients of the antennas by a matched filter so that the contribution of all the antennas can be summed in the end obtaining the image with the magnitude of the detected targets greater than the background magnitude. With this algorithm it is possible to reconstruct 2D images.

The distance of the antennas to each pixel in the region of interest can be calculated with:

$$dist = || Pos_{Antenna} - Pos_{Pixel} || \quad (2.12)$$

Where $Pos_{Antenna}$ and Pos_{Pixel} are the antenna position and pixel position respectively.

As the electric field expression for the antenna is calculated with Equation 2.13 it is possible to cancel the phases of the reflected electromagnetic waves by multiplying this field by a matched filter with opposite phase as it is shown in Equation 2.14.

$$E = E_0 e^{-2jk_0 ndist} \quad (2.13)$$

$$MF = e^{2jk_0 ndist} \quad (2.14)$$

Where k_0 is the wave number calculated as $\frac{2\pi}{\lambda}$ and n is the refractive index of the propagation medium.

After this multiplication the electric field will be approximately zero if there is no target and a constant with the value $Number\ of\ antennas \times E_0$ if there is a target.

The attained image can be described by the equation 2.15:

$$\sum_{n=0}^{N_a} \sum_{x=0}^{N_x} \sum_{y=0}^{N_y} \Gamma_L(n, x, y) \times MF(n, x, y) \quad (2.15)$$

Where N_a represents the number of antennas, N_x the number of pixels in the x direction, N_y the number of pixels in y direction and Γ_L the reflection coefficients of each antenna.

A schematic of this algorithm can be depicted in the figure below:

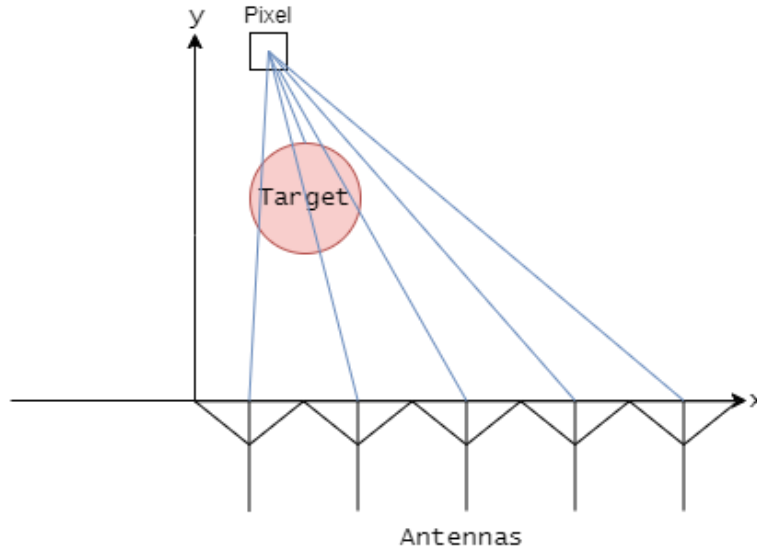


Figure 2.8. Description of the image reconstruction algorithm

In this figure, there are five antennas sweeping a region of interest that contains several pixels that will have different reflection coefficients according to the position of each one, there is a target that will influence these reflection coefficients and will be visible in the reconstructed image.

As observed in the previous chapter, the refractive index varies in the regions 0, 1, and 2. Consequently, this must be reflected in the image algorithm. In the x direction, the refractive index will be the same in all three regions to maintain the continuity of evanescent fields. In the z direction, the refractive index will be that of the medium itself, well-defined by the material of each medium and its boundaries. This can also be expressed in polar coordinates, where radially, the refractive index will be the refractive index of the medium, and tangentially, it will be the same in all media. This representation of the refractive index is very useful when conducting a circular antenna sweep around the breast.

Therefore, the expression for the distance ($dist$) with the index of refraction (n) in equation 2.15 will be as follows:

$$ndist = n_{breast} \times d_{breast} + n_{air} \times d_{air} + n_{lens} \times d_{lens} \quad (2.15)$$

Where n_{breast} , n_{air} and n_{lens} are the indexes of refraction of breast tissue, air and the dielectric slab (lens) and d_{breast} , d_{air} and d_{lens} are the distances travelled inside each medium by the electromagnetic wave.

To account for the tangential refractive index, the following geometry was considered:

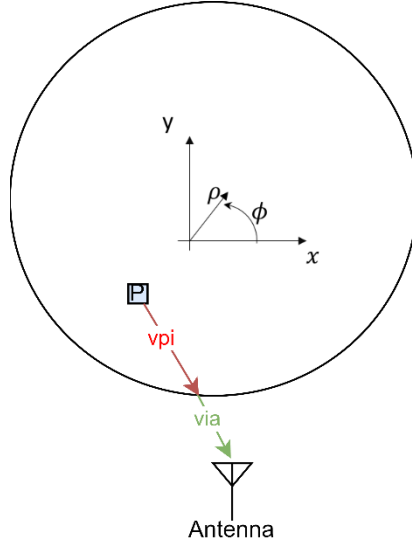


Figure 2.9. Geometry for the tangential refractive index algorithm

The vectors \vec{v}_{pi} \vec{v}_{ia} are the vectors between the pixel and the breast interface, breast interface and antenna respectively.

In this geometry, it is possible to differentiate the radial and tangential refractive indices by calculating the distance and considering the refractive index in each component of each vector, obtaining equation 2.16.

$$ndist_v = \sqrt{n_r \times v_r + n_t \times v_t} \quad (2.16)$$

where n_r is the radial coordinate of the refractive index, n_t is the tangential coordinate of the refractive index, and v_r and v_t are the radial and tangential components of each vector.

2.3 Image quality metrics

In order to evaluate the quality of the reconstructed image there are two types of metrics that can be used, the first type is image quality metrics, where the imaging detection quality is evaluated, and tumor detection metrics, where the ability of the image to detect the correct position of the tumor is evaluated. In these two types of metrics there are some quantitative figures of merit that are used:

For the imaging quality metrics:

TCR (tumor-to-clutter ratio) and TMR (tumor-to-mean ratio) are used to quantify how good the image represents the tumor in relation to the background clutter (unwanted artifacts). These figures of merit are calculated using the following equations (in linear units):

$$TCR = \frac{\max(T)}{\max(C)} \quad (2.9)$$

$$TMR = \frac{\max(T)}{\text{mean}(C)} \quad (2.10)$$

Where T represents the intensity of the tumor response and C the intensity of the clutter response.

For the tumor detection metrics:

PE (positioning error) is used to quantify the distance between the real position of the tumor and the detected position, it can be calculated using the following expression:

$$PE = ||P_{tumor} - P_{detected}|| \quad (2.11)$$

Where P_{tumor} is the real position of the tumor and $P_{detected}$ is the detected position.

There is also another figure of merit related to the PE, which is the NPE (normalized positioning error), that is the positioning error normalized to the theoretical resolution of the system, NPE can be calculated using the following expression:

$$NPE = \frac{PE}{\Delta d} \quad (2.12)$$

Where PE is the positioning error calculated with equation 2.11 and Δd is the theoretical resolution of the system, calculated using equation 2.13 [8]:

$$\Delta d = \frac{c}{4n_b^{avg} \Delta f} \quad (2.13)$$

Where c is the speed of light in vacuum, n_b^{avg} is the average of the refractive index of the breast tissues in a frequency band and Δf the bandwidth of the system.

All these figures of merit can be applied after obtaining the reconstructed image with the algorithm presented in chapter 2.2.

3 State of the art

This chapter aims to provide an overview of the current state of the art in microwave imaging systems, highlighting the most recent developments and trends in this field. It begins with a brief review of the basic principles of microwave imaging, followed by a discussion of the various techniques and technologies that are currently being used to produce high-resolution microwave images. Then it is presented the current state of the art in super-resolution microwave imaging, highlighting the most recent developments and trends in this field. It begins with a review of the basic principles of super-resolution imaging, followed by a discussion of the various techniques and technologies that are currently being used to produce high-resolution microwave images.

3.1 Microwave imaging for breast cancer

Microwave imaging systems became to appear in the 1960s through the development of the radar and other similar sensors. These systems have multiple applications such as earth observation, weather forecasting, environmental monitoring, and medical imaging where microwaves are used to non-invasively detect and measure the properties of tissues of the human body.

The operating principle of these systems is based on the contrast between the permittivity of the different tissues in the breast. One or more antennas capture the electromagnetic energy that is scattered by these tissues.

Most of today's microwave imaging systems use frequencies in the band of 1GHz-10GHz (ISM band), there are certain constraints on the selection of frequencies, as a low frequency may result in a low resolution, while a high frequency may not be able to effectively penetrate the breast[6]–[8]

There are multiple systems that use microwave imaging in controlled setups with a liquid that is used to do coupling with the measuring antennas [6], more recently there are studies revolving dry setups as these are more comfortable to the patient and there is no need to submerge the breast in a liquid [8].

There are two types of microwave imaging systems, monostatic systems where the same antenna is responsible for the transmission and reception of the signals and multistatic systems where a single antenna transmits a signal and multiple antennas receive it at different locations. Examples of these systems are represented in Figure 3.1 for monostatic systems and Figure 3.2 for multistatic systems.

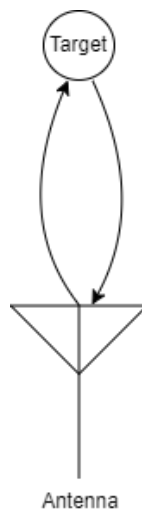


Figure 3.1: Monostatic system

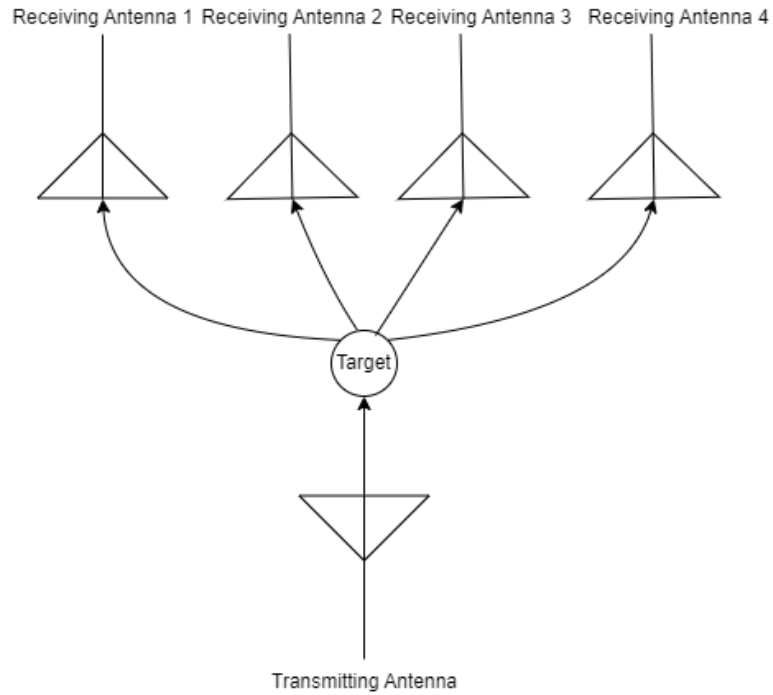


Figure 3.2: Multistatic system

At the Instituto de Telecomunicações, work on microwave imaging for breast cancer with dry setups has been developed. To simulate breast tissues, a shell is filled with TX-100, a liquid with electromagnetic properties similar to those of the tissues found in the breast at the frequencies of interest. To simulate tumors, 3D printing using PLA filament has been utilized [7], [8].

Two antenna types were utilized: the XETS (cross exponentially tapered slot-based antenna) and the BAVA (balanced antipodal Vivaldi antenna). The XETS exhibits an extremely stable phase center across its entire frequency range of operation, while the BAVA is broadband and straightforward to manufacture [15]. The following figures show these antennas.

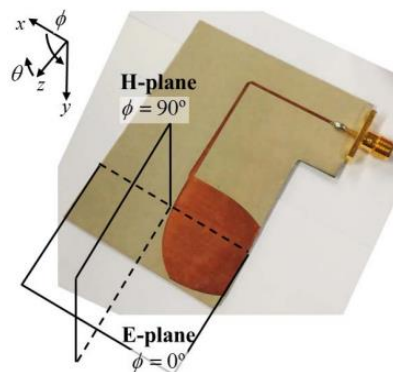


Figure 3.3. BAVA Antenna (extracted from [15])

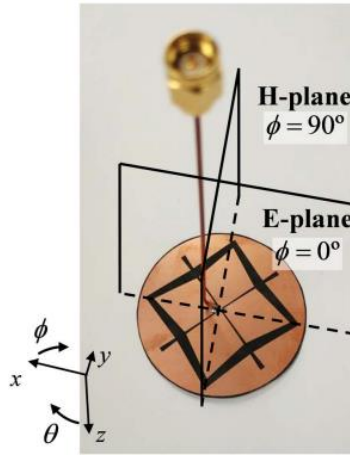


Figure 3.4. XETS Antenna (extracted from [15])

Utilizing the XETS the obtained results were positive for tumors of large size but not that good for small tumors (inferior to 3mm), as it can be seen by the Figure 3.5 and Figure 3.6.

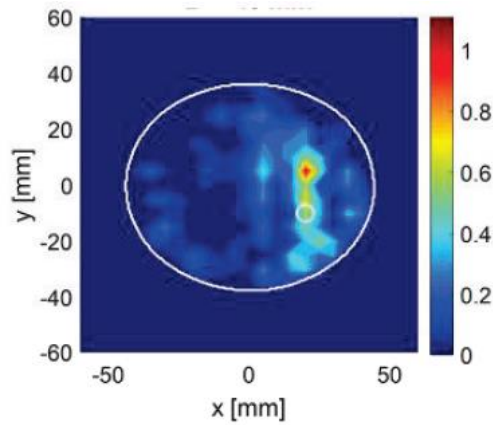


Figure 3.5. Reconstructed image for 3mm tumor (extracted from [7])

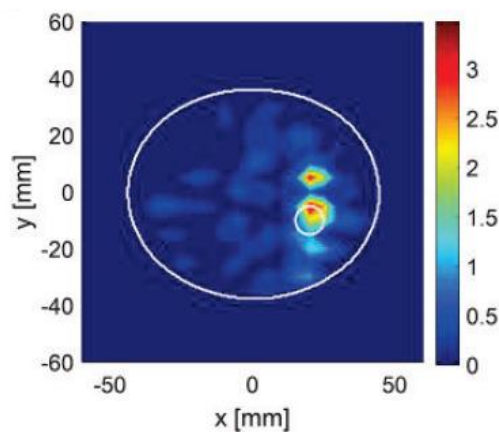


Figure 3.6. Reconstructed image for 5mm tumor (extracted from [7])

The poor results for small tumors are attributed to the limitation of current systems by Rayleigh diffraction. To address this issue, techniques such as super lenses are utilized to enhance the resolution of the acquired images.

3.2 Super-resolution Imaging

Super-resolution imaging is a set of techniques used to produce images with higher resolution than is possible with conventional imaging methods, breaking the Rayleigh's diffraction limit. This limit states that every imaging system that uses electromagnetic waves is limited to a resolution of $\lambda/2$, this happens because electromagnetic waves have a finite wavelength and when the size of the objects being imaged is smaller than half of the wavelength of operation it is not possible to represent them.

These techniques have been developed and refined over the past several decades and have found a wide range of applications in fields such as medicine, microscopy, and engineering[16]–[19].

Some authors ([18]–[22]) use machine learning approaches to increase the resolution of imaging systems, these approaches were proven to produce high resolution images, and are compatible with any conventional inverse scattering algorithm, such as the one presented in chapter 2, but they have a major limitation which is the need to have a very extensive dataset to train the convolutional neural networks.

The physical approaches are more reliable because they don't need any previous knowledge of information about position of tumors or another data to train the neural networks.

Other authors [23]–[25] use complex materials with negative permittivity, obtaining decent super-resolution results. However, the materials used are quite complex to construct, and some of them are not suitable for the frequency band utilized in these kinds of applications [26].

One of these physical approaches ([27]) uses a metamaterial dielectric slab (which is a type of slab made from a material that has been artificially engineered to have specific electromagnetic properties that are not found in natural materials) with a high relative permittivity by stacking printed circuit boards with certain properties, and it was verified experimentally that the resolution increases with these types of super lenses.

To test the validity of the lens, two setups were carried out. The first setup consisted of a dipole horizontally traversing the lens with two targets behind it, and the second setup involved the same configuration but without the lens, to determine whether it was possible to detect the two targets. The results obtained are shown in Figure 3.7.

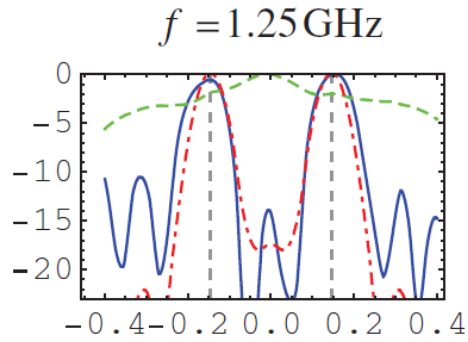


Figure 3.7. Reflection coefficient in function of position (extracted from [27])

In Figure 3.7, the magnitude of the reflection coefficient is shown as a function of the dipole position (normalized to the wavelength). The dotted grey line represents the true position of the two targets. The dotted green line indicates the result without the application of the lens, as can be seen it is not possible to detect the two targets without the lens. The blue line represents the result with the application of the lens, it is possible to see the well-defined detection of the two targets, with the S11 maxima in the target zone. The dotted red line represents the theoretical result calculated by the authors, which is very similar to the experimental result obtained in blue.

4 Numerical and Simulation Results

In this chapter, the numerically obtained results are explored and interpreted through simulations. These results are aimed at verifying the theoretical concepts of super-resolution and determining the feasibility of detection within a breast. This examination sets the stage for potential experimental testing of these setups.

4.1 Super-resolution validation and imaging

To validate the state-of-the-art results on super-resolution [10], a comparable scenario was tested. Using CST [28], a simulation was conducted for a similar setup as depicted in Figure 4.1.

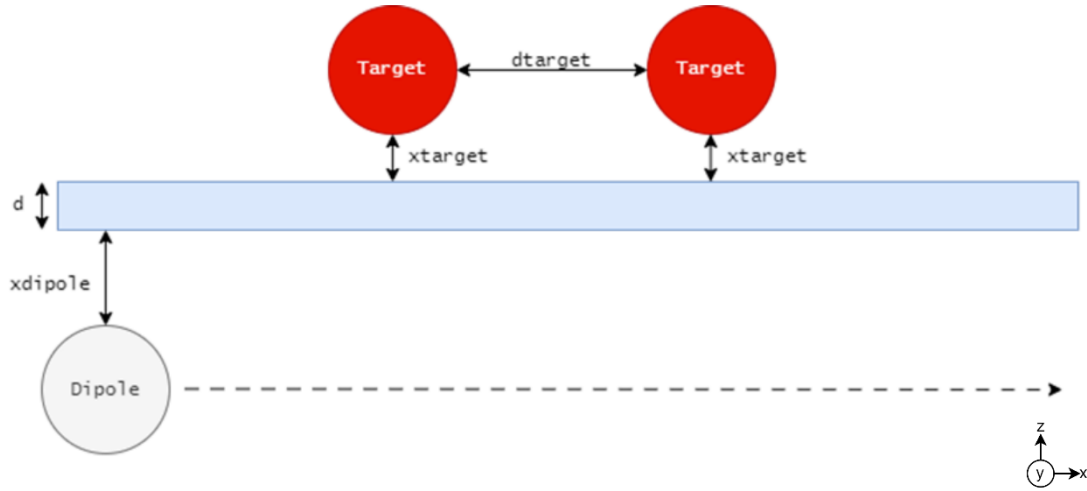


Figure 4.1. Geometry of the simulations for super resolution validation

In Figure 4.1 it is represented the generic geometry of multiple setups, with a lens of thickness d two targets with a distance d_{target} between them and x_{target} between each one to the lens, a dipole with a distance x_{dipole} from the antenna to the lens.

With this geometry four setups were made:

- Dipole in free space with no targets
- Dipole in free space with two targets
- Dipole with a lens and no targets
- Dipole with a lens and two targets

To verify the efficacy of the proposed microwave imaging system, various experimental configurations were designed and implemented. A lens of thickness $d = 1\text{ mm}$, determined using Equation 2.4, was utilized in these simulations. A scan was done on the x-axis, varying the position of the antenna by 5 mm in 5 mm in a region of -100 mm to +100 mm. These configurations were chosen to study the performance of the imaging system under a range of different conditions and to validate the theoretical concepts presented in Chapter 2.

Using MATLAB[29], the S parameters were extracted from the CST [28] simulation, encompassing the responses of both the targets, the lens and the antenna. In order to obtain the reflection coefficient of the targets only, it was necessary to calibrate the S11 parameter. Knowing that the S11 obtained from the simulations of the dipole in free space with two targets contains the reflection coefficient of the antenna and the target, and that the S11 obtained from the simulations of the dipole in free space with no target contains the reflection coefficient of the

antenna, it becomes trivial to obtain only the S11 of the target, by subtracting the S11 of one simulation from the other.

The following graph was then obtained, presenting the calibrated S11 as a function of position (in x), for a frequency of 5.5 GHz which is the resonant frequency of the utilized dipole.

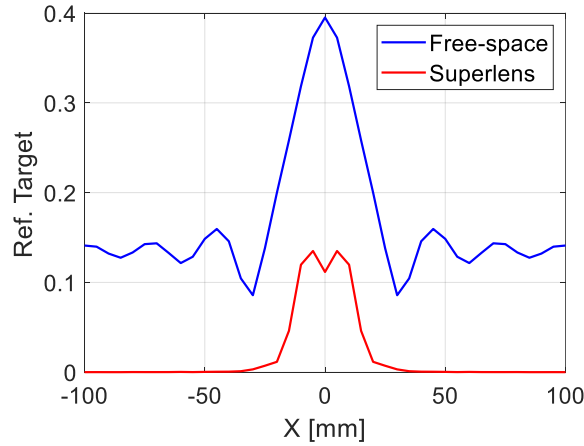


Figure 4.2. Super Resolution with water lens and dipole

For the generation of this graph, the utilized setup is illustrated Figure 4.3 with $d = 1 \text{ mm}$ (to propagate only one mode within the dielectric slab), a lens permittivity of 78 (employing a water lens with losses), $x_{dipole} = 3.5 \text{ mm}$, $x_{target} = 3.5 \text{ mm}$, and $d_{target} = 8.63 \text{ mm}$ (equivalent to approximately $\lambda/6$ in free space). As depicted in Figure 4.2, in the case of testing detection in free space, it is evident that no distinction can be made between the two targets. This is attributed to the electromagnetic wave being constrained by Rayleigh diffraction. However, when the water lens is introduced (serving as a dielectric slab due to its significantly high permittivity), despite obtaining a response with lower amplitude (attributed to the substantial losses in water), a distinction between the targets at the correct positions (with $d_{target} = 8.63 \text{ mm}$) becomes perceptible. Consequently, the results observed in the state-of-the-art are validated.

To utilize the image reconstruction algorithm, it is necessary to calculate the refractive indices, in the x and z direction. In this case, the refractive index in z direction will be the refractive index of the medium itself. For the analysis of distance in free space, $n = 1$, and for the analysis of distance within the lens, $n = \sqrt{78}$ (refractive index of water) is considered. To calculate the refractive index, in the x direction, the following setup was simulated, as depicted in Figure 4.3, in two situations. The first involves placing an embedded active dipole within the water lens, and another passive dipole serving as a target at 10mm. The second situation excludes the consideration of the passive dipole, leaving only the lens and the active dipole. In these simulations, the S11 parameters were exported to calculate the target response as a function of distance (by subtracting the S11 from the simulation with both dipoles from the S11 of the simulation with only the active dipole). This approach allows for the calculation of the electrical distance between dipoles, visualizing the distance corresponding to the maximum intensity of the target response.

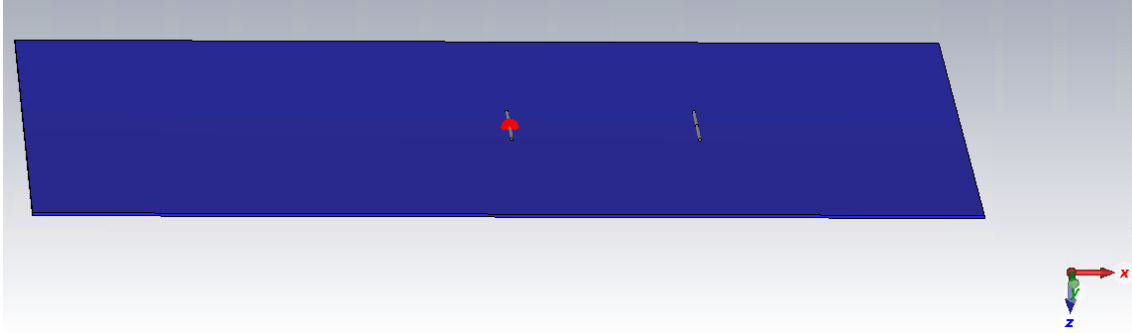


Figure 4.3. Setup for the n_x calculation

With this setup, it was obtained the following graph with the target response which is the difference between S11 with active dipole, lens, and passive dipole and S11 with active dipole and lens in function of the distance:

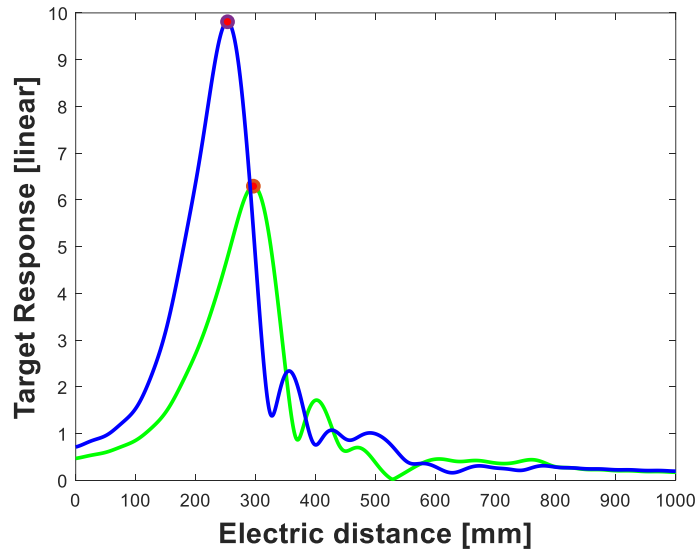


Figure 4.4. Target response in function of the electric distance

In Figure 4.5, the blue curve represents the response of the target with the passive dipole placed 50mm from the active dipole, while the green curve represents the response with the passive dipole placed 60mm from the active dipole. The electrical distances (which are a measure of the phase shift experienced by the wave) obtained are 253 mm for the blue curve and 296 mm for the green curve. These electrical distances correspond to the distances at which the maximum reflection intensity is detected. In both situations, the active dipole is positioned at the center of the slab. The refractive index according to x is calculated using the following expression:

$$n_x = \frac{d_{e1} - d_{e0}}{d_1 - d_0} \quad (4.1)$$

Where d_{e1} and d_{e0} are the electrical distances of the further and closest position of the target respectively and d_1 and d_0 are the physical distances of the further and closest position of the

target respectively. With this expression, the refractive index in the x direction is approximately 4.3.

With the refractive index calculated in both directions, it is now possible to employ the image reconstruction algorithm explained in section 2.2, resulting in the following images:

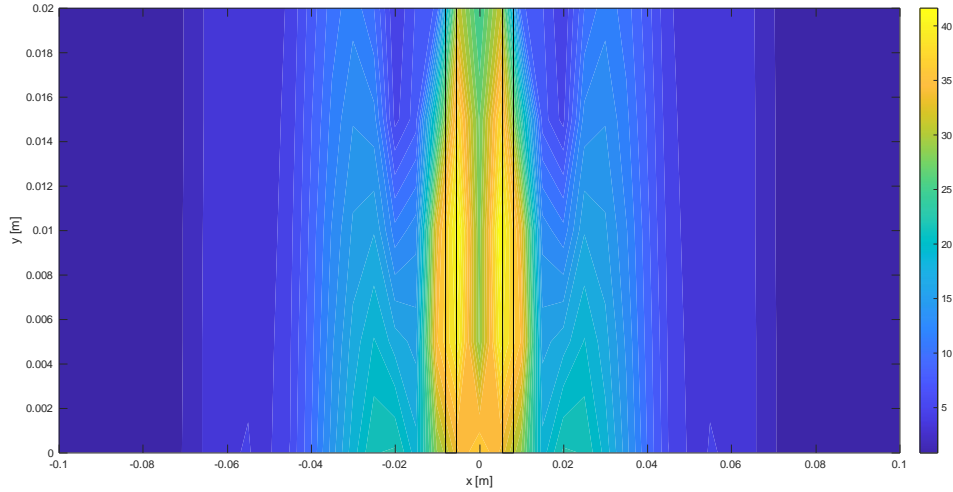


Figure 4.5. Obtained image with the algorithm, with lens

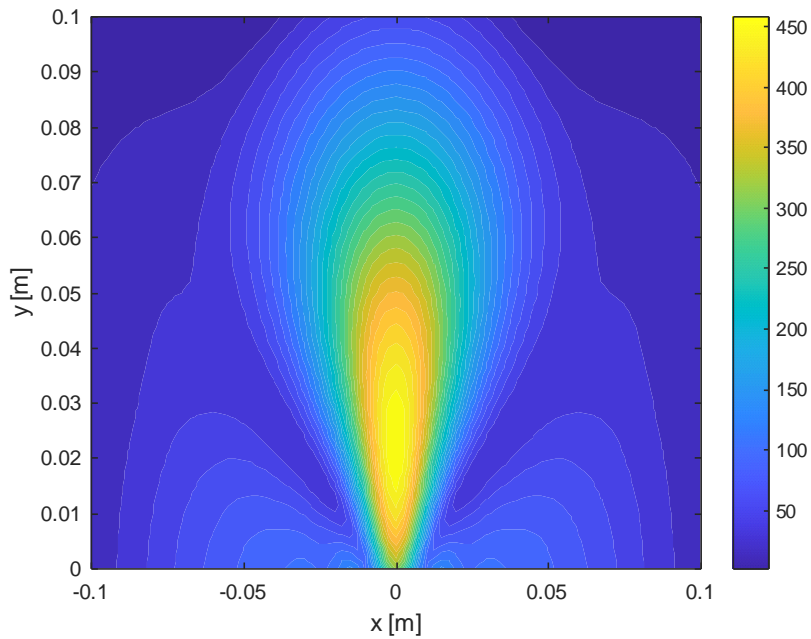


Figure 4.6. Obtained image with the algorithm, in free space

In the image, a distinction among the targets is evident when the lens is present, revealing a separation between the targets ($dtarget$) of 8.63 mm. This differentiation is not observed when the targets are in free space, where there is no distinction between the targets, resulting in a merging of the responses of both targets at the center of the image.

4.2 Super Lenses Simulation inside breast

To simulate the super lenses, the theoretical study was initially verified in the simulation, and subsequently, the detection of targets was tested using the image reconstruction algorithm presented in Chapter 2.

4.2.1 Lens Attenuation

To verify the calculations of attenuation in an asymmetric dielectric slab (as is the case in the final setup, where medium 0 is air, medium 1 is the lens with a permittivity approximately equal to 78, and medium 2 is the breast with a permittivity approximately equal to 4), a simulation was performed. A setup was created with a dipole placed 2 mm from the lens, operating at 6 GHz, a water lens (permittivity equal to 78), and a parallelepiped representing the breast material (permittivity = 4) immediately following the lens, as depicted in Figure 4.7 and Figure 4.8

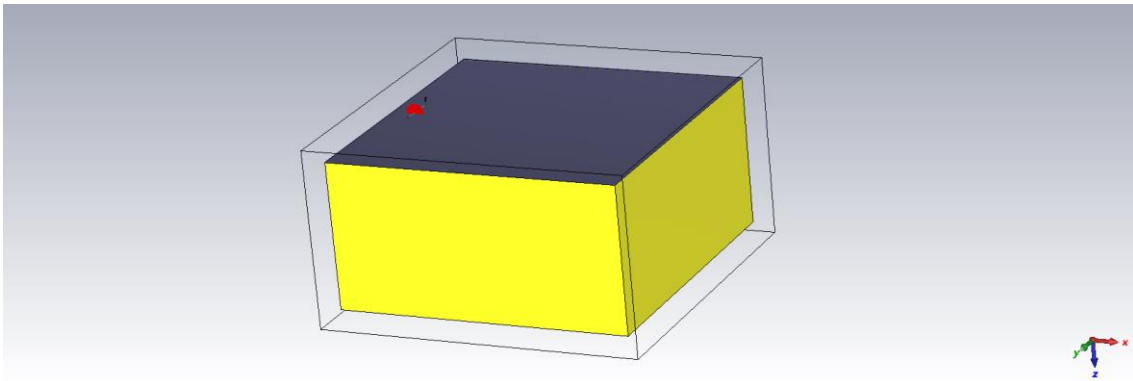


Figure 4.7. Setup of the attenuation simulation (perspective view)

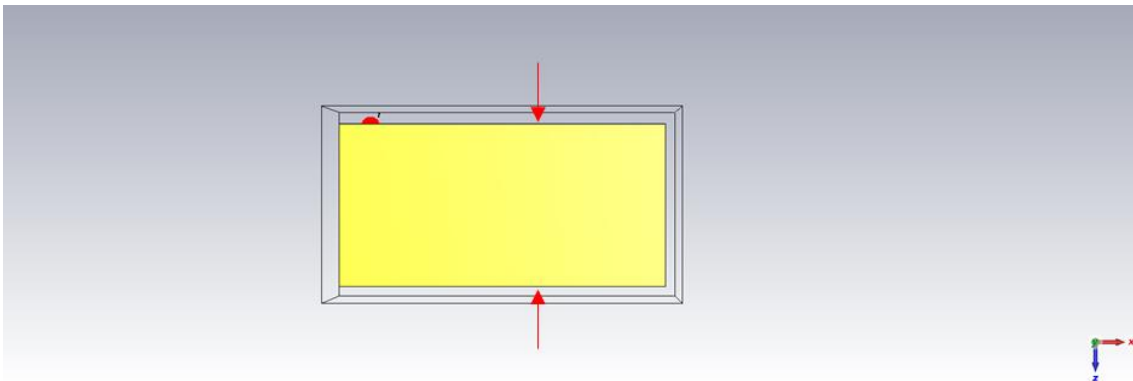


Figure 4.8. Setup of the attenuation simulation (front view)

Four scenarios were simulated:

- Dipole with a lens of thickness 1mm and permittivity 78.
- Dipole with a lens of thickness 1mm and permittivity 60.
- Dipole with a lens of thickness 0.5mm and permittivity 78.
- Dipole with a lens of thickness 0.5mm and permittivity 60.

In this setup, the near-field electric field was simulated as a function of distance in the z-direction, assuming a constant x of 20 mm from the center of the lens (marked by the red arrows, in the front view). it was defined an attenuation as:

$$Att = |20 \log(E[p1]) - 20 \log(E[p2])| \quad (4.2)$$

Where E[p1] and E[p2] are the values of the RMS near field for z = 1 mm and z=2 mm respectively.

With this equation it is possible to plot the Attenuation in function of frequency obtaining the following graphs for different values of slab thicknesses and permittivity.

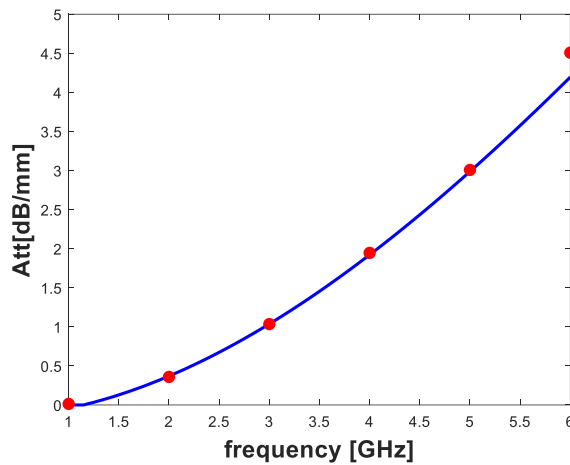


Figure 4.9. Attenuation for a lens with thickness = 1 mm and permittivity = 78

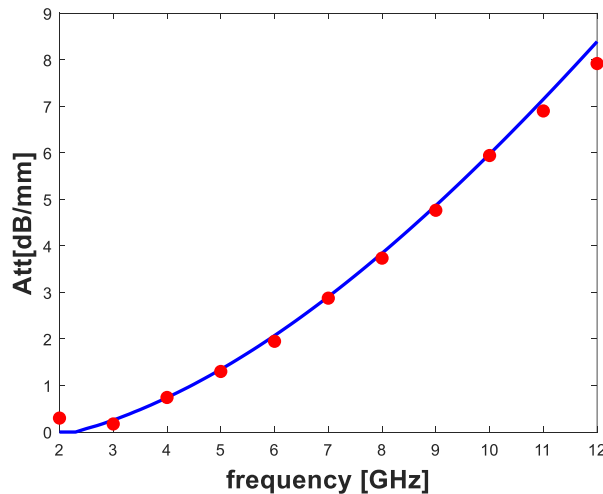


Figure 4.10. Attenuation for a lens with thickness = 0.5 mm and permittivity = 78

In these two figures, the blue line represents the value calculated using equation 2.11, and the red line represents the simulated and calculated value using equation 4.3. It can be concluded that for both scenarios, the simulation value is approximately equal to the theoretically calculated value, thus confirming the equations empirically.

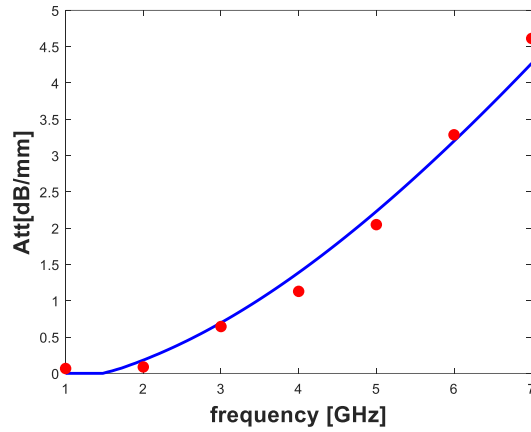


Figure 4.11. Attenuation for a lens with thickness = 1 mm and permittivity = 60

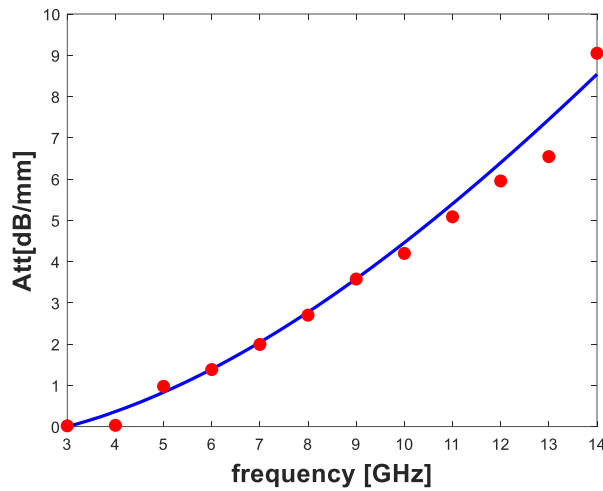


Figure 4.12. Attenuation for a lens with thickness = 0.5 mm and permittivity = 60

Once again, it is concluded that empirical results validate theoretical equations, indicating an increase in attenuation with frequency in all cases, as well as an increase in attenuation with the permittivity of the slab. The frequencies chosen for plotting these graphs are those for which only one mode propagates in each of these slabs, calculated using equations 2.7 and 2.8 and defined in the table below.

		d	
		1	0.5
ϵ_r	78	[1.1028;6.2415]	[2.2056;12.483]
	60	[1.4512;7.1880]	[2.9024;14.376]

Table 4.1. Bandwidth of monomodal propagation

The bandwidth for each scenario is measured in gigahertz (GHz), and as observed in the table, dielectric slabs with smaller thicknesses can provide twice the bandwidth where only one mode propagates. This bandwidth will increase with a decrease in the permittivity of the slab.

As seen in the table above and in Chapter 2, there are frequencies where no mode propagates in the dielectric slab. This is verified through simulation in CST by configuring the setup as depicted in Figure 4.13.

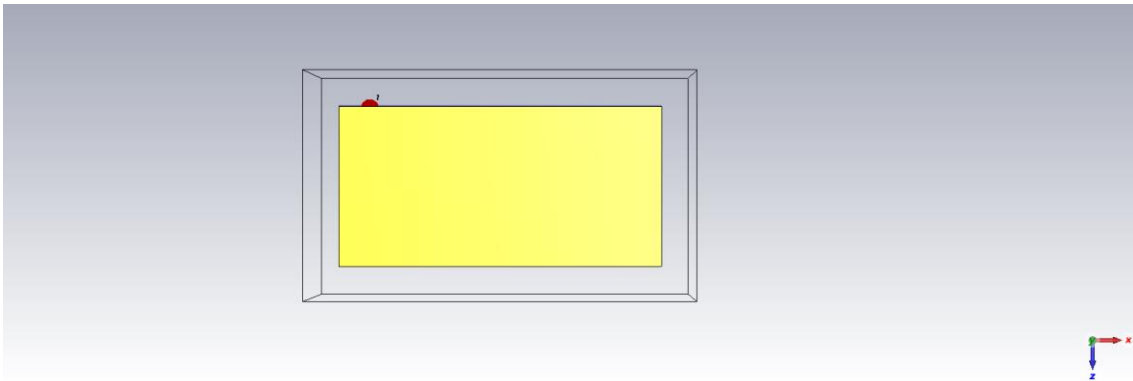


Figure 4.13. Setup for propagation validation

In this setup, a dipole designed at 5.5 GHz was placed entirely embedded in the lens, 15mm from the beginning of the lens (in the x-direction) with a thickness of 1mm and permittivity of 78. A parallelepiped with breast properties and a thickness of 100 mm (permittivity equal to 4) was then simulated for the electric field at $y=0$ in two situations: the first for a frequency of 500 MHz, where no mode is expected to propagate, and the second for a frequency of 5 GHz, where a mode propagates within the slab. The results are presented in the figures below.

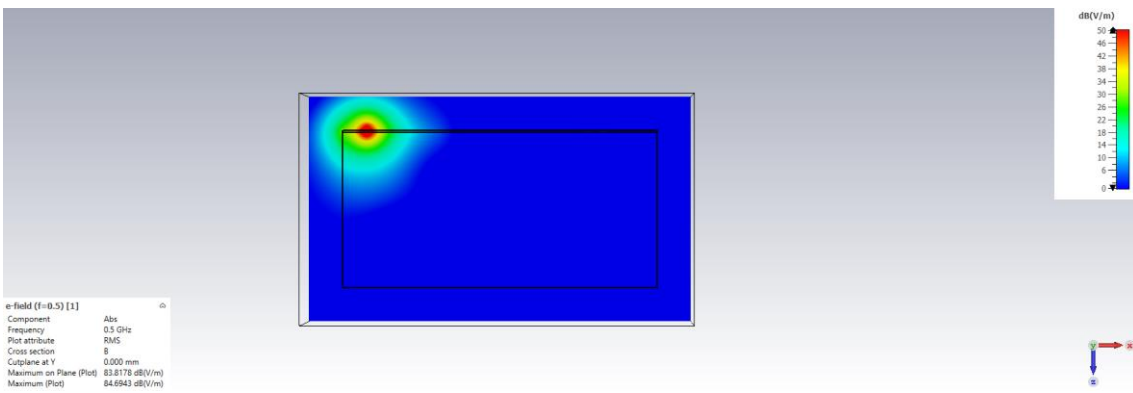


Figure 4.14. Propagation inside the slab at 500 MHz

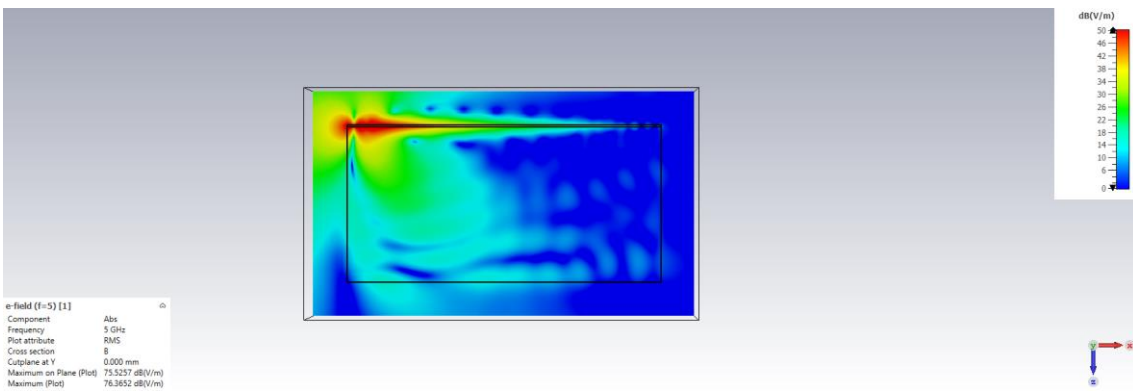


Figure 4.15. Propagation inside the slab at 5 GHz

As seen in the figures above, for a frequency outside the propagation bandwidth of the slab (500MHz), no mode propagates within the slab, indicated by a null electric field. However, for 5GHz, propagation within the slab is evident from the electric field, which is highly confined within.

4.2.2 Super-resolution Detection Simulation

Prior to conducting any experimental tests, simulations were necessary to determine if it was possible to detect small superficial tumors. To achieve this, CST was used, utilizing a dielectric slab of water (permittivity 78) with a thickness of 1mm, placed above a 20 mm slab with a permittivity of 4, representing the breast. A dipole designed for 5.5 GHz was positioned 2 mm away from the lens (in the z-direction), and two PEC (Perfect Electric Conductor) cylinders were embedded in the breast with a spacing of 14 mm between them at depths ranging from 0 to 4 mm, to test the detection capability, this setup is represented in Figure 4.16.

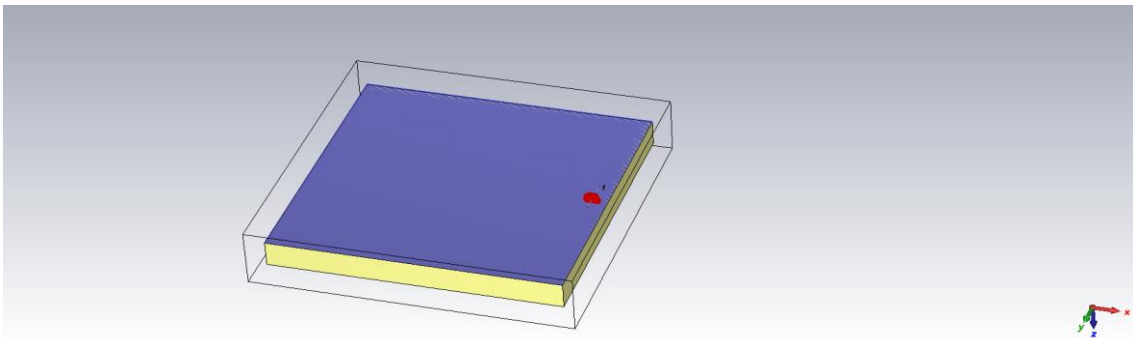


Figure 4.16. Detection Simulation Setup

As explained in Chapter 2, the refractive index in the x-direction differs from the refractive index in the z-direction, and to calculate this refractive index, an algorithm was developed to determine the optimal values for each frequency, as this index varies with frequency. In this algorithm, the actual positions of the targets are known in advance, and a 1D image is generated for various refractive indices. Subsequently, the algorithm compares the position where the maximum reflection intensity exists (the presumed location of the targets) with the actual positions of the targets. The chosen refractive index is the one for which the difference between the actual positions of the targets and the detected positions is minimized. This process is tested in frequency bands of 100 MHz, assigning a refractive index to each of these bands. Finally, a curve fitting is performed to represent the refractive index curve as a function of frequency. An example of a 1D image tested for one of the selected refractive indices is presented in Figure 4.18. The results of this algorithm for the simulation are presented in the figure below.

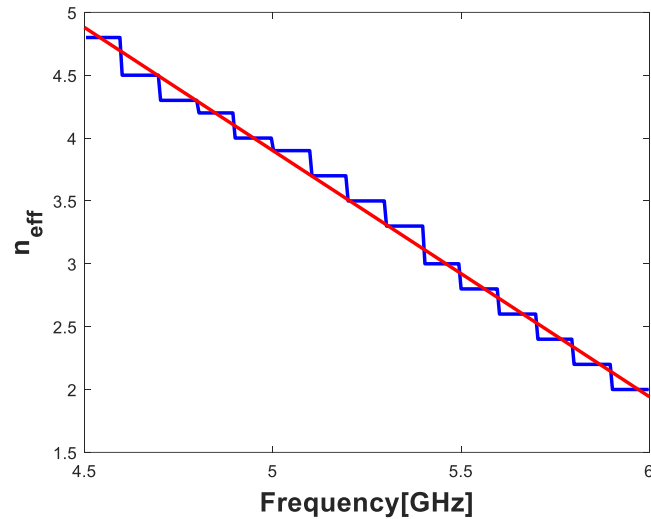


Figure 4.17. Variation of n_x with frequency for slab thickness of 1 mm

In the figure, the blue line represents the outcome of the algorithm selecting the refractive index in the x-direction as a function of frequency, while the red line represents the result of the curve fitting. As observed in the above result, the refractive index in the x-direction decreases with frequency, maintaining approximately the same slope. This indicates the propagation of a single mode within the slab.

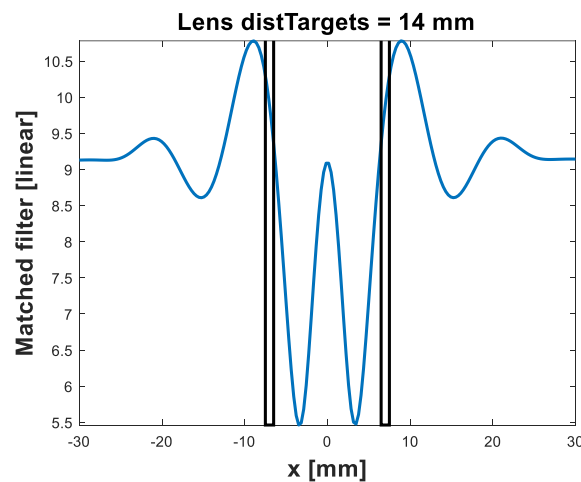


Figure 4.18. 1D Image for $z=0$ and slab thickness of 1 mm

In this figure, the targets are depicted as black bars, and the blue curve represents the detection results with the image algorithm conducted at $z = 0$, where the targets are located. As observed in the image, the position at which the targets are being detected is very close to their actual position, with the minimum difference between these positions occurring in a frequency band ranging from 5.9 to 6 GHz. This results in a refractive index in the x-direction of 2, as depicted in Figure 4.17.

Using this algorithm for refractive index selection and the image reconstruction algorithm, images were generated for depths ranging from 0 to 4 mm and for two slabs with a permittivity of 78,

varying the thickness from 1 mm to 0.5 mm. The results for the first slab (thickness = 1 mm) at depths of 0, 1, 2, and 3 mm are presented in Figure 4.19, Figure 4.20, Figure 4.21 and Figure 4.22, respectively.

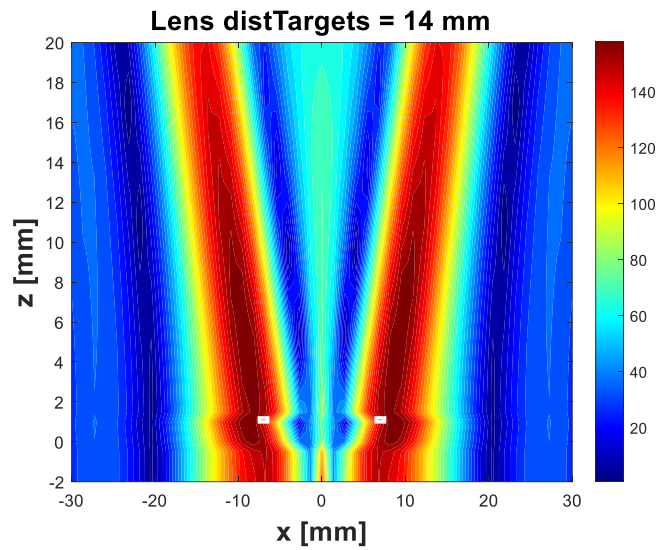


Figure 4.19. 2D Image for depth = 0mm and slab thickness of 1 mm

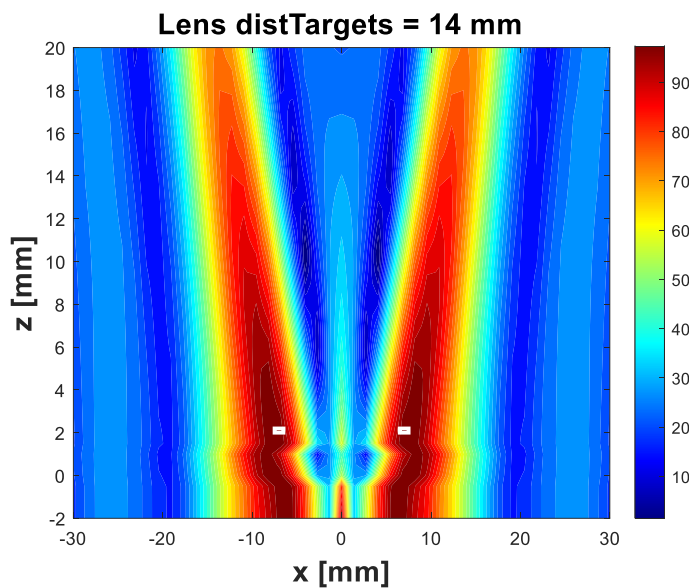


Figure 4.20. 2D Image for depth = 1mm and slab thickness of 1 mm

In these first two images, where the depth is 0 and 1 mm, it is possible to observe the detection of two targets in the correct positions, with a distance between targets of 14 mm (less than $\frac{\lambda}{2}$ in the breast, surpassing the Rayleigh diffraction limit). There is also a decrease of 50 in linear units, equivalent to an attenuation of approximately 2 dB/mm, which is roughly in line with the theoretical calculations.

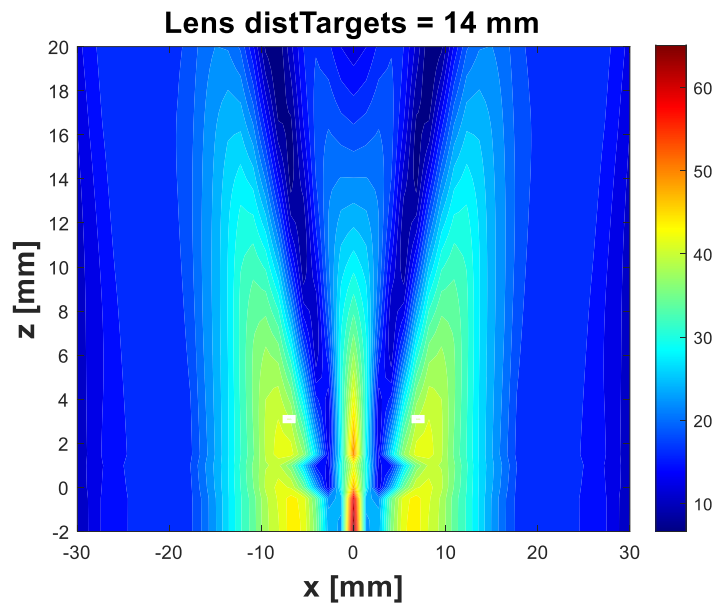


Figure 4.21. 2D Image for depth = 2 mm and slab thickness of 1 mm

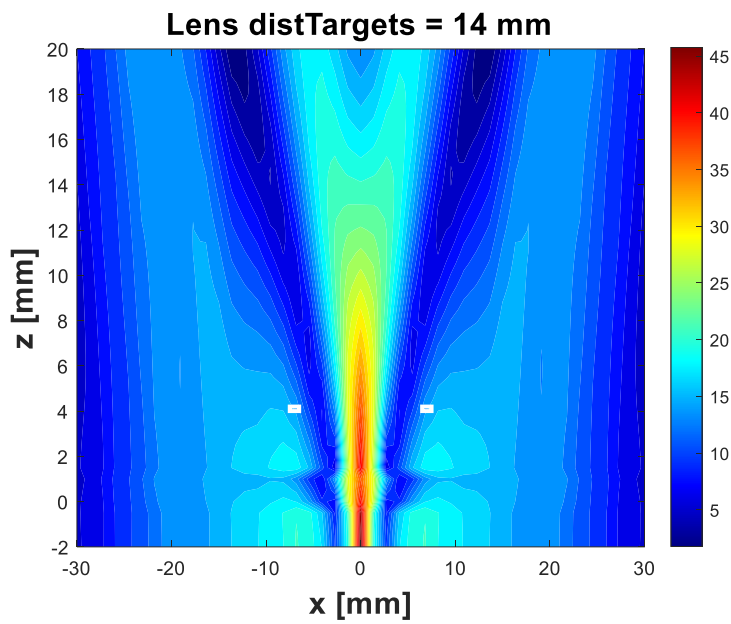


Figure 4.22. 2D Image for depth = 3 mm and slab thickness of 1 mm

Based on the results obtained from a depth of 3 mm, it is no longer possible to detect tumors separated by 14 mm, as the responses of both tumors are summed in the center of the image. This further confirms the attenuation of 2 dB/mm obtained in the previous figures, affirming the detection capability primarily for superficial tumors.

As done for the 1 mm-thick slab, the approximation algorithm was applied to the results with the 0.5 mm-thick plate, this time extending the frequency up to 7 GHz, as this plate supports higher frequencies where it operates in a single-mode manner. The results are shown in the figures below:

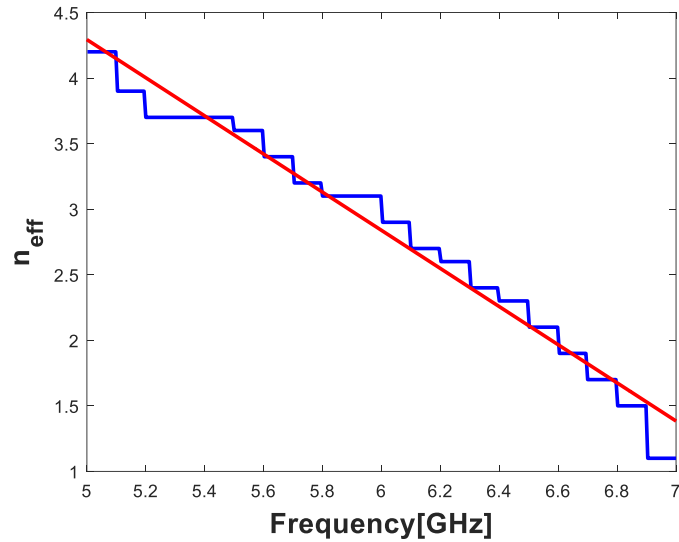


Figure 4.23. Variation of n_x with frequency for slab thickness of 0.5 mm

Similar to Figure 4.17, in this figure, the blue line represents the outcome of the algorithm selecting the refractive index in the x-direction as a function of frequency, while the red line represents the result of the curve fitting. The same decrease in the refractive index with frequency is observed, with a constant slope.

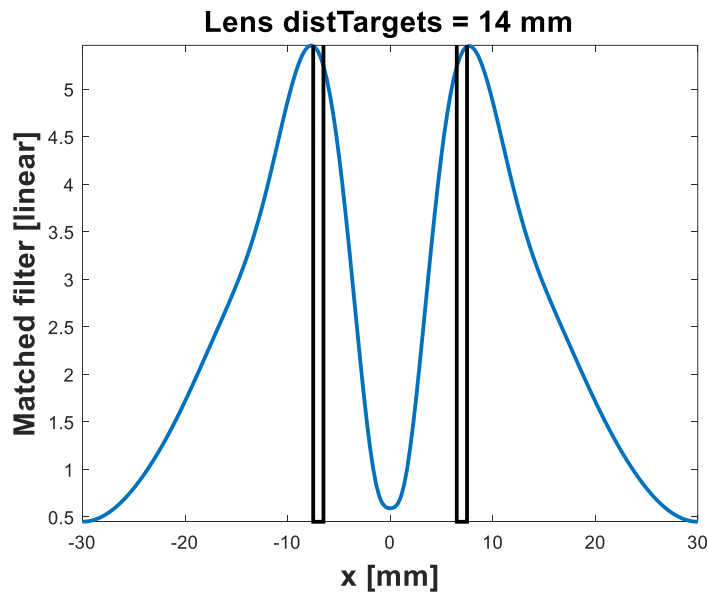


Figure 4.24. 1D Image for $z = 0$ and slab thickness of 0.5 mm

In this figure, similar to Figure 4.18, the targets are represented by the black bars, and the blue curve represents the detection results with the image algorithm conducted at $z = 0$, where the targets are located. As observed in the image, the positions where the targets are being detected are very close to their actual positions, with the minimum difference between these positions occurring in a frequency band ranging from 6.9 to 7 GHz. This results in a refractive index in the x-direction of 1.1, as depicted in Figure 4.23.

The 2D images generated with the image reconstruction algorithm and the refractive index selection algorithm in the x-direction are presented for the same depths as the 1 mm-thick slab, which are 0, 1, 2, and 3 mm, in Figure 4.25, Figure 4.26, Figure 4.27 and Figure 4.28, respectively. This was done to assess if there would be any significant advantage in resolution by reducing the slab thickness, thereby enabling the use of higher frequencies.

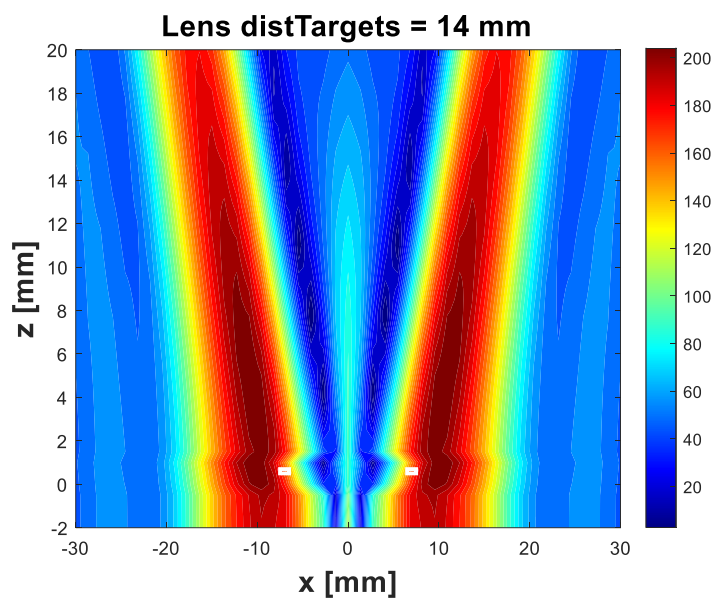


Figure 4.25. 2D Image for depth = 0 mm and slab thickness of 0.5 mm

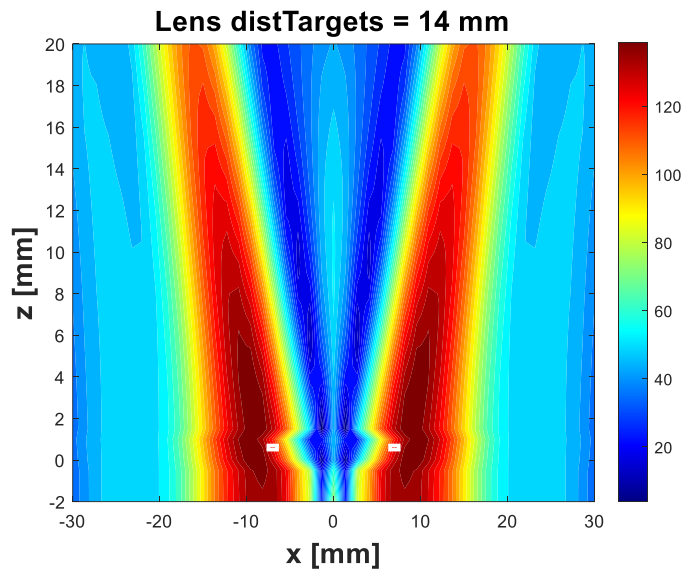


Figure 4.26. 2D Image for depth = 1 mm and slab thickness of 0.5 mm

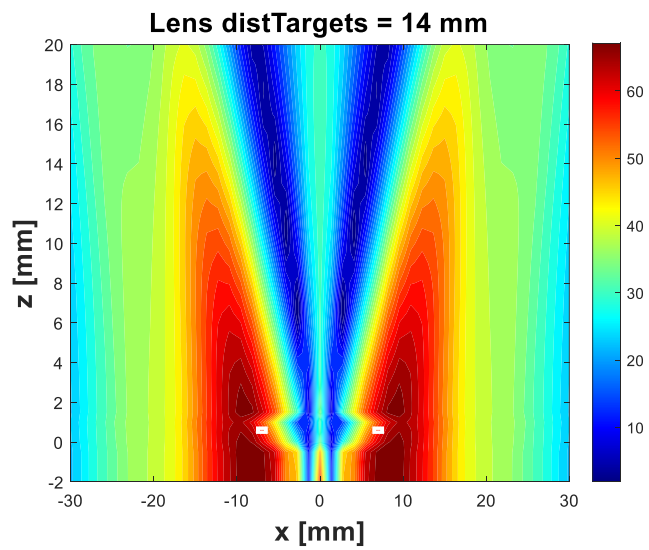


Figure 4.27. 2D Image for depth = 2 mm and slab thickness of 0.5 mm

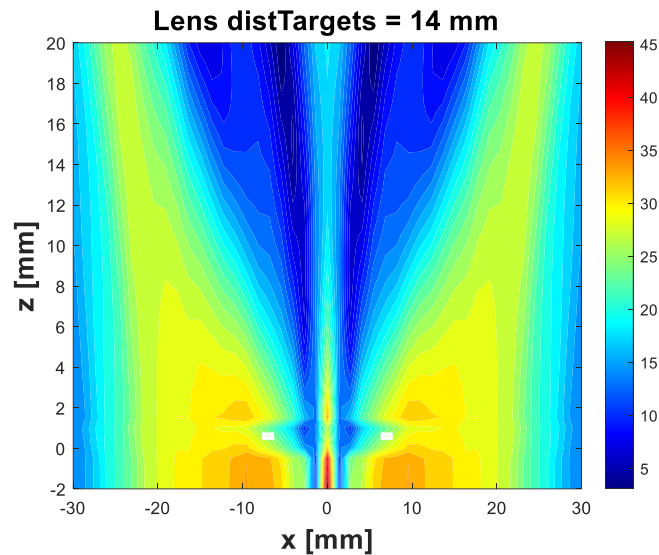


Figure 4.28. 2D Image for depth = 3 mm and slab thickness of 0.5 mm

The results obtained for the 0.5mm dielectric slab are similar to those obtained with a 1 mm thickness, resulting in slightly lower attenuation, at 1.9 dB/mm. However, detection is achievable up to a depth of 2 mm, similar to what was observed with the thicker slab. It is therefore concluded that, for these frequencies, there is no significant advantage in reducing the thickness of the slab, as similar results are obtained with both slabs.

Since in a real situation, the breast is more similar to a cylinder than a parallelepiped, the following structure, as represented in the figure below, was simulated. In this structure, the breast is represented by a cylinder with a radius of 50 mm and a height of 100 mm. A dielectric slab in the shape of an arc is placed around the breast, and a dipole designed for 5.5 GHz is positioned 2 mm away from the lens. The dipole performs a circular sweep around the breast, scanning the breast over 180 degrees and taking measurements every 6 degrees. Two PEC targets are embedded, spaced 10 mm apart, and placed at a depth of 0mm in the first simulation and 1 mm in the second simulation. The same scenarios were also simulated without the lens for comparison. The setup for a depth of 0 mm, with a 1 mm-thick lens and permittivity of 78, is depicted in the figure below.

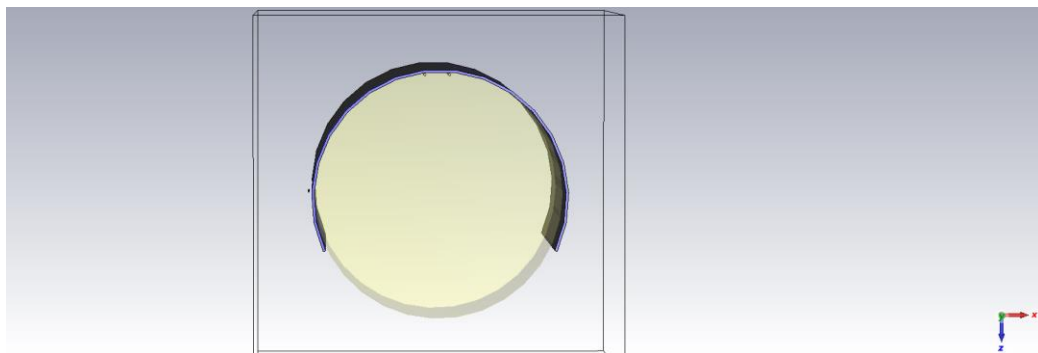


Figure 4.29. Setup for cylindrical breast

The same process of selecting the refractive index in the x-direction was carried out for a frequency band, resulting in the following figures:

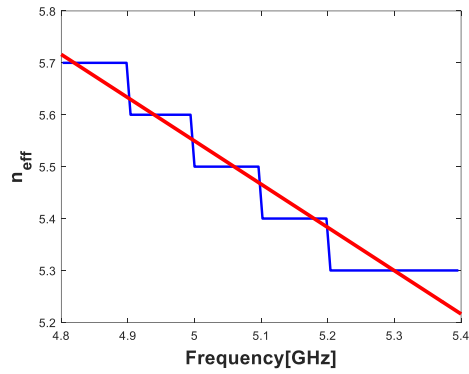


Figure 4.30. Variation of n_x with frequency for slab thickness of 1mm and cylindrical breast

As seen previously, once again, there is a decrease in the refractive index with frequency, with a constant slope. The red curve represents the curve used for the refractive index in the x-direction, which is used in the image reconstruction algorithm.

After obtaining the refractive index in the x-direction, the image reconstruction algorithm was used to generate a 2D image. These results are presented in Figure 4.31 and Figure 4.32 for setups without the lens and with the lens, respectively.

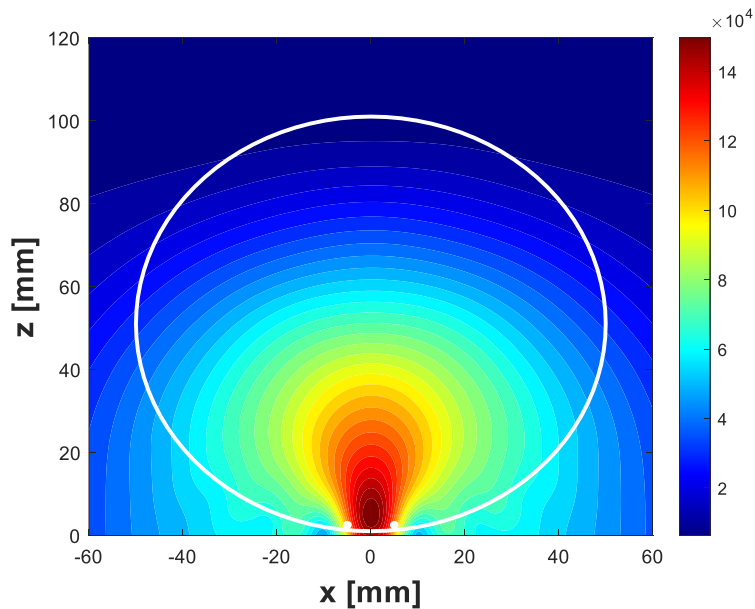


Figure 4.31. 2D Image for detection with no lens

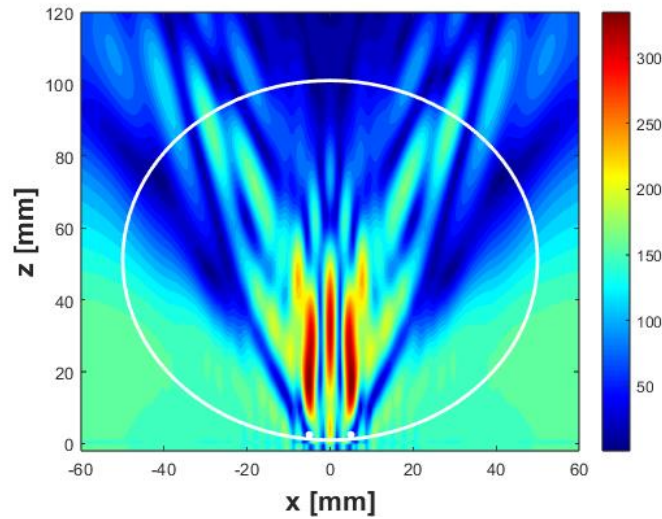


Figure 4.32. 2D Image for detection with lens for a depth of 0 mm

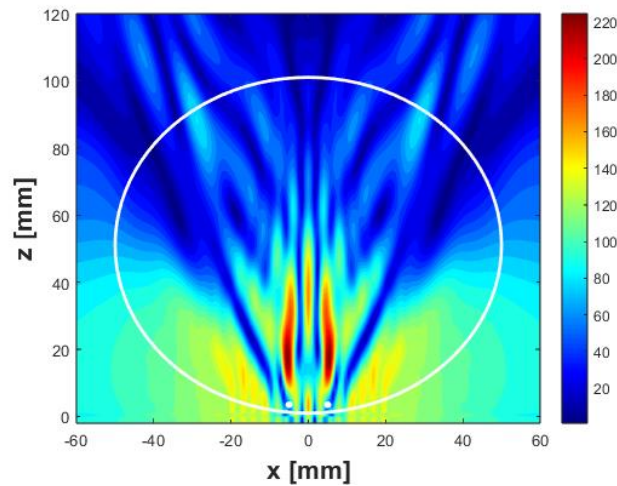


Figure 4.33. 2D Image for detection with lens for a depth of 1 mm

From the images above, it is possible to observe that without the lens, there is no detection, with the response of the two targets interacting in the center of the image. With the lens, detection is achieved between targets spaced 10 mm apart. When the targets are placed at a depth of 1 mm, a decrease in amplitude from 300 to 220 is observed, which translates to an attenuation of approximately 1.4 dB/mm. This result is very similar to what was theoretically expected for this frequency band.

5 Experimental Results

The Experimental Results chapter explores the practical testing and outcomes detailed within the thesis. It aims to assess the performance of the theories previously explored in real-world scenarios. By conducting meticulous experiments and analysis, this chapter is designed to present actual evidence, examining how theoretical ideas and simulations manifest in actual situations.

5.1 Detection with symmetrical slab

Several experimental tests were conducted to validate the numerical and simulated results. Prior to any experimental testing, various materials were examined for their suitability in creating a high-permittivity solid lens. Three materials were proposed, including agar (a polysaccharide commonly used in culinary applications to make gelatin) ultrasound gel, and aloe vera gel. The permittivity and conductivities of these three materials were tested to determine if they possessed the desired properties for constructing the lens, using the Coaxial probe method [30]. The results of the permittivity and conductivities are presented in the figures below for all three materials.

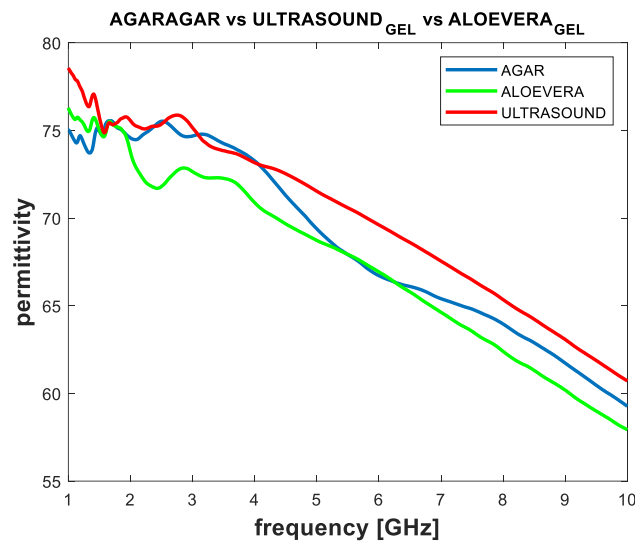


Figure 5.1. Permittivity vs frequency for Agar, Aloe vera Gel and Ultrasound Gel

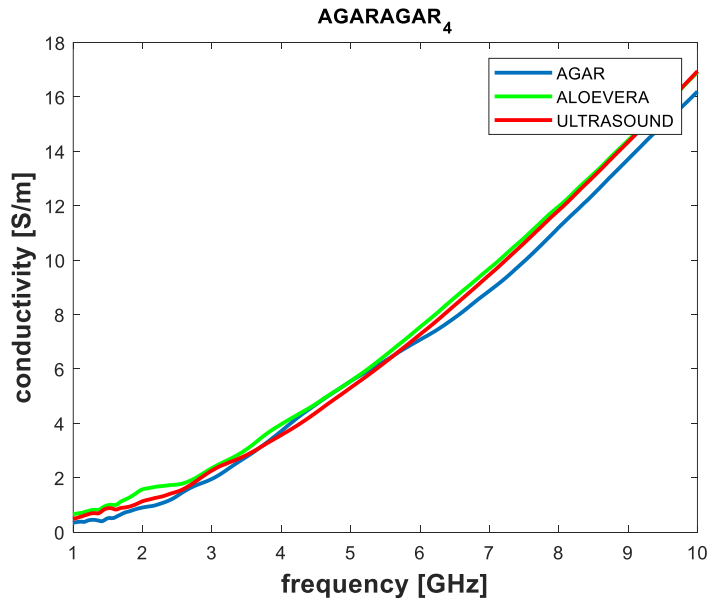


Figure 5.2. Conductivity vs frequency for Agar, Aloe vera Gel and Ultrasound Gel

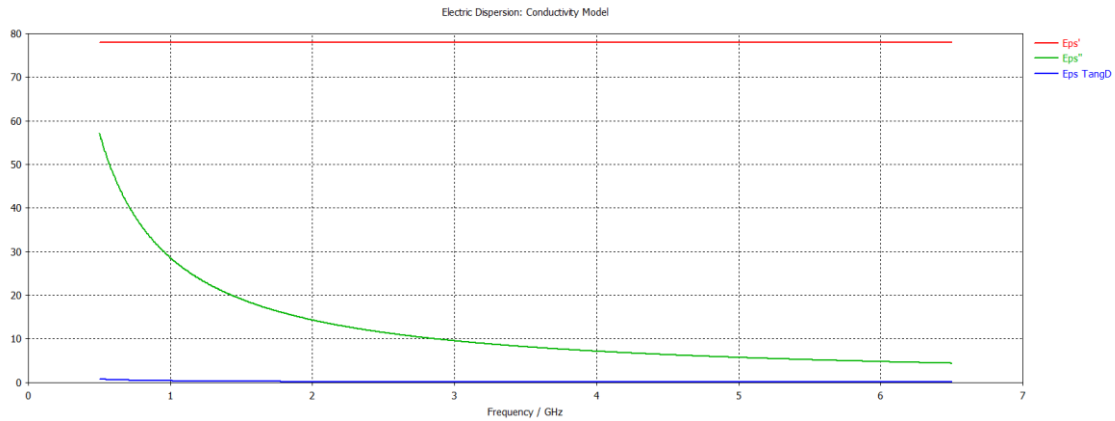


Figure 5.3. Permittivity and $\tan\delta$ of water

These results were generated to enable comparison with the permittivity of water (presented in Figure 5.3), to determine if they were good candidates for use as lenses to achieve super-resolution. It is the high permittivity that allows for the creation of evanescent fields not physically constrained by Rayleigh diffraction.

Based on these results, it is possible to conclude that all of these materials could be potential solutions for creating the lens, as their permittivity is very close to that of water, effectively functioning as dielectric slabs.

These three materials were subsequently tested for manufacturing a dielectric slab. However, it was observed that aloe vera gel was a low-viscosity material, resulting in a very liquid lens that made measurements difficult. Therefore, the decision was made to exclude this material, and lenses were fabricated using the remaining materials.

To create the agar lens, a frame measuring 180x180x1 mm was 3D printed, using PLA, to hold the lens structure. This frame was attached to an acetate sheet. Then, a homogeneous solution was prepared with 6 g of agar powder and 250 ml of water. The solution was heated until it began to boil and was poured into the frame. Finally, another acetate sheet was placed over the frame, covering the homogeneous solution, and the mixture was evenly spread.

For the ultrasound gel lens, ultrasound gel was applied over an identical frame with the acetate sheet attached underneath. Another acetate sheet was placed on top to spread the gel uniformly.

The first experimental test served as a proof of concept, aiming to verify the detection in symmetric dielectric slabs and compare these results with those obtained through simulation. The setup used closely resembled the one utilized in the simulations, involving a dipole located approximately 2mm from the lens, designed for 6 GHz, with the same orientation of the targets. The targets employed consisted of two aluminum pieces, each with a thickness of approximately 0.1 mm and a width of 1 mm, mirroring the simulation conditions. These targets were tested for various values of distTargets (target separation). The setup is depicted in Figure 5.4 and Figure 5.5 for the configurations without a lens and with a lens, respectively.

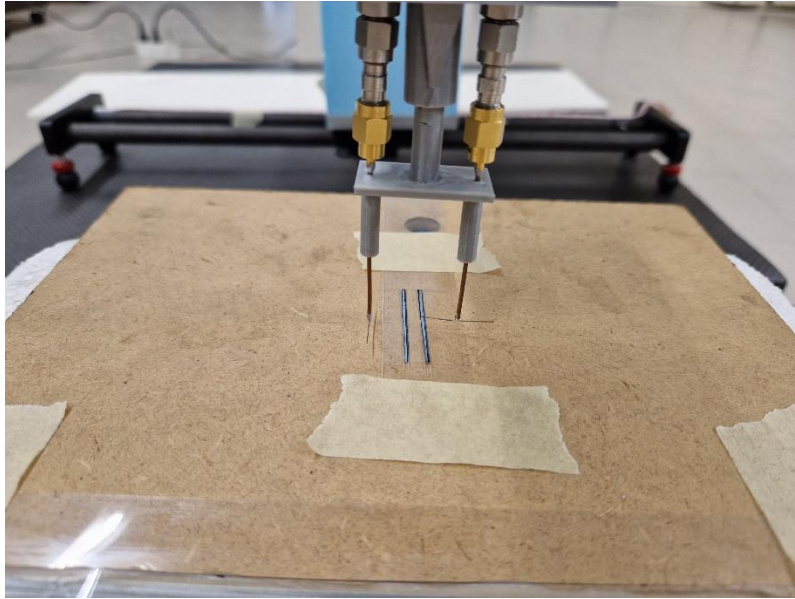


Figure 5.4. Experimental setup (without lens) for symmetrical slab

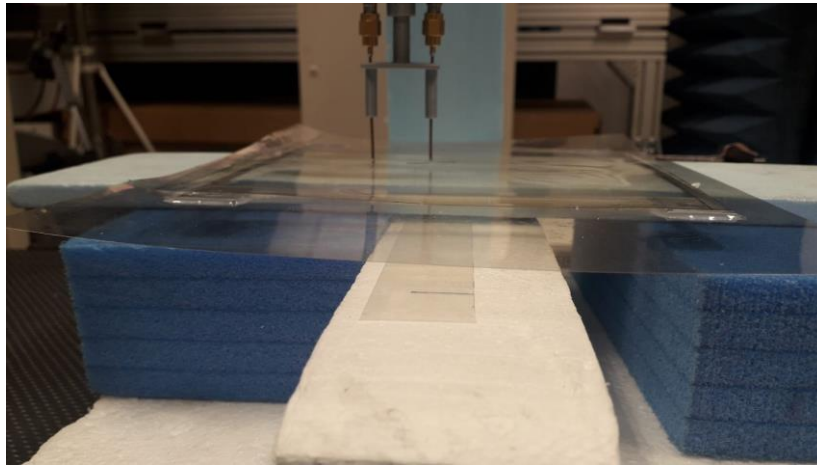


Figure 5.5. Experimental setup (with lens) for symmetrical slab

With the setups depicted in the figures above, measurements of the S_{11} were conducted, mirroring the simulation approach, but this time utilizing a Vector Network Analyzer (VNA). For Figure 5.7, Figure 5.8 and Figure 5.9, the lens used was the agar lens, whereas for figures Figure 5.10 and Figure 5.11, the lens utilized was the ultrasound gel lens. Distances between targets of 14, 9, and 5.5 mm were tested with lens, and 14 mm without lens. The results are presented in the figures below.

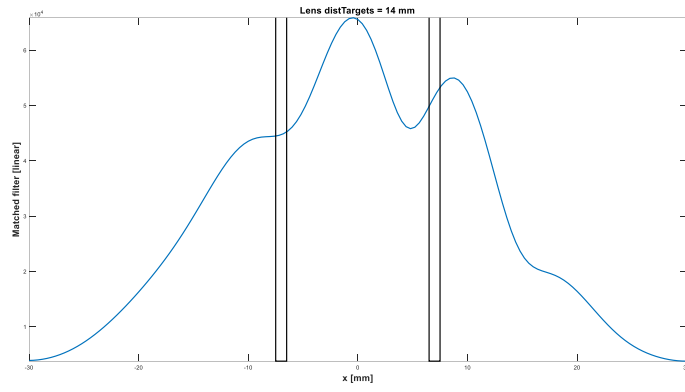


Figure 5.6. Image without lens with distTargets = 14 mm

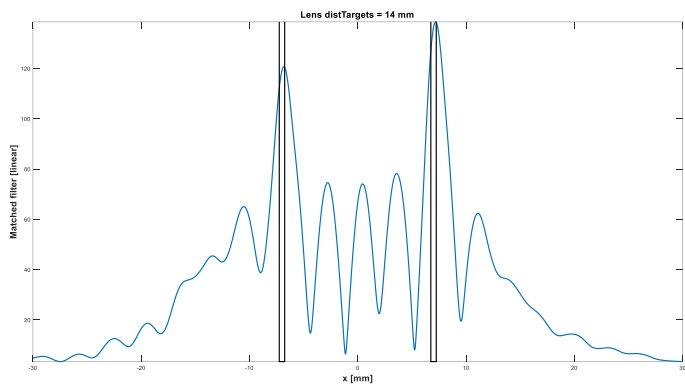


Figure 5.7. 1D Image for Agar Lens with distTargets = 14 mm

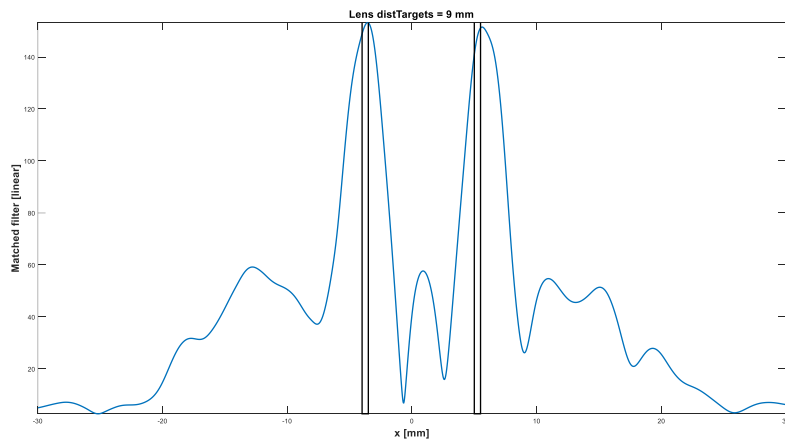


Figure 5.8. 1D Image for Agar Lens with distTargets = 9 mm

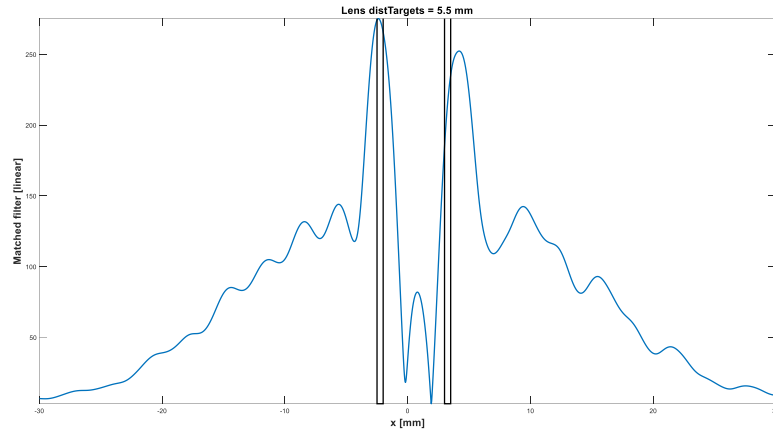


Figure 5.9. 1D Image for Agar Lens with distTargets = 5.5 mm

In all these images, the frequency band used ranged from 5 to 6 GHz (where only one mode propagates within the slab). Based on the results obtained, it is possible to observe detection in all three cases with the lens, for the different separation distances. This is not observed in the case where the setup does not have a lens, as it is limited by Rayleigh diffraction. The maximum resolution that could be achieved without a lens in this case would be 50 mm ($\frac{\lambda}{2}$). As a result, no resolution is obtained for separation distances between targets that are less than this value, as seen in Figure 5.6.

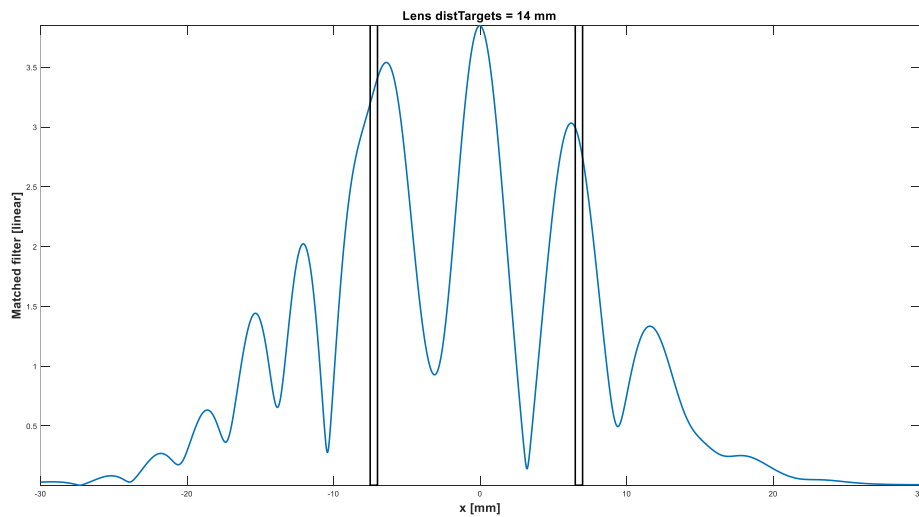


Figure 5.10. 1D Image for Ultrasound Gel Lens with distTargets = 14 mm

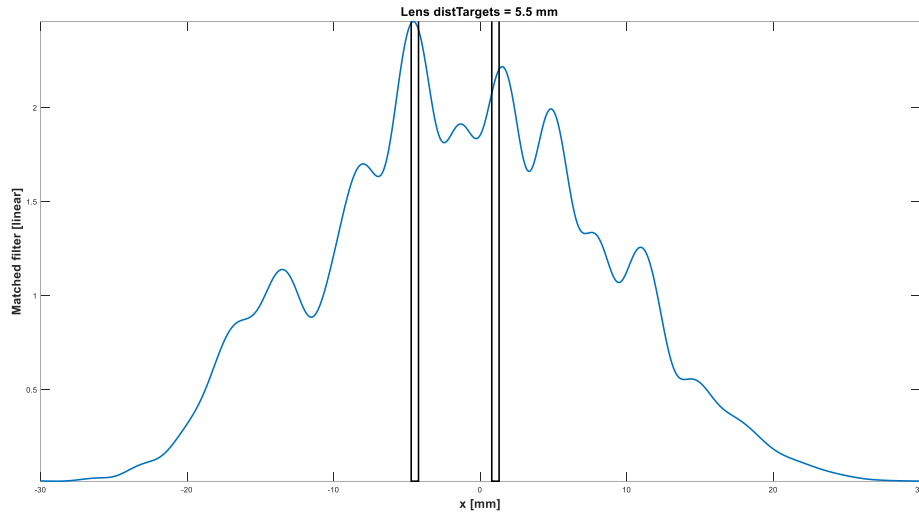


Figure 5.11. 1D Image for Ultrasound Gel Lens with $\text{distTargets} = 5.5 \text{ mm}$

For the ultrasound gel lens, the conclusions are similar (targets can be detected up to a 5.5 mm separation). However, there is a much greater interaction between the targets compared to the agar lens. This may be attributed to various factors, such as the ultrasound gel lens being a less homogeneous structure compared to the agar lens. Ultrasound gel is more viscous and less easily spread than agar, when agar is in a liquid state which complicates the process of fabrication of this lens.

5.2 Detection with asymmetrical slab

To experimentally test an asymmetric dielectric slab setup, a CD case was filled with Triton X-100, a laboratory detergent that simulates the electromagnetic properties of breast tissue (with a permittivity approximately equal to 4)[31]. An agar lens, fabricated in the same manner as the symmetric setup, but with a frame, 3D printed with TPU, so it can be bended and attached to the CD case using adhesive tape, as observed in Figure 5.13, Figure 5.14 and Figure 5.15. The used antenna was a dipole designed for 4.9 GHz. The dipole swept through an angle range of 315° to 45° around the CD case. Tumors were represented by cylindrical metal rods with a 6 mm diameter, placed at center-to-center separations of 30 mm, 20 mm, and 10 mm and at depths of 0 mm, 7 mm, and 14 mm within the case representing the breast.

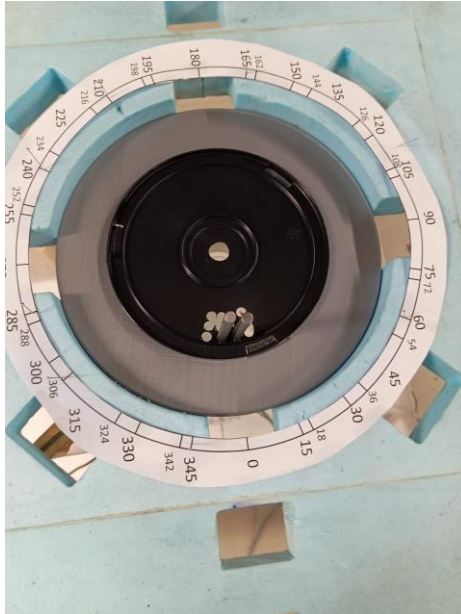


Figure 5.12. Setup for Radial measurements

As observed in the image above, the targets are centered at 0° . The CD case was perforated to allow the placement of the metal rods at different positions and depths, with the aim of testing detection in various scenarios, mirroring the simulations conducted and presented in Chapter 4. The figures below depict the front view of the setups used for measurements with target separations of 30, 20, and 10 mm. Figure 5.13, Figure 5.14 and Figure 5.15 correspond to setups with an agar lens, while Figure 5.16, Figure 5.17 and Figure 5.18 represent setups without a lens.

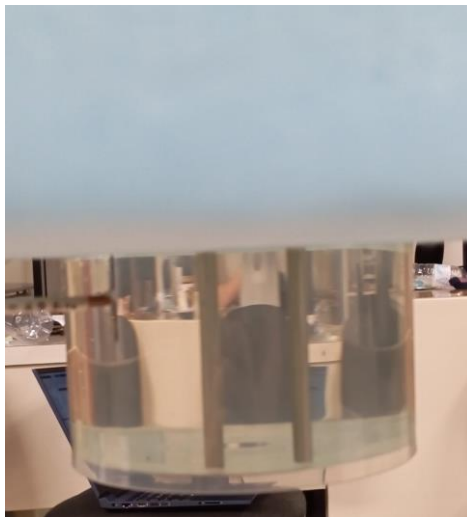


Figure 5.13. Front view for radial setup with lens and $\text{distTargets} = 30$ mm

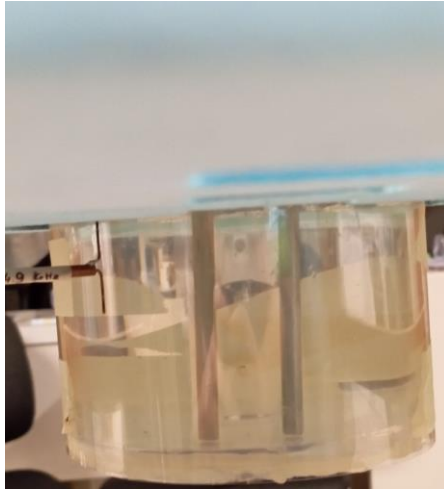


Figure 5.14. Front view for radial setup with lens and distTargets = 20 mm

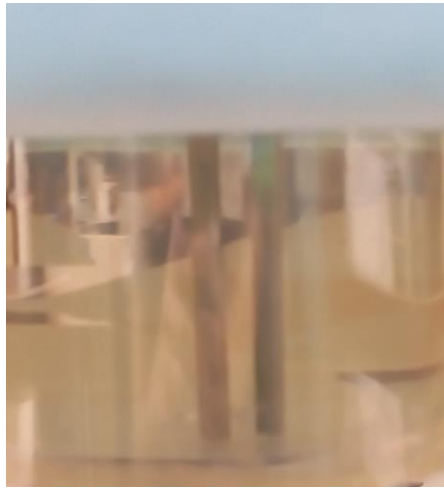


Figure 5.15. Front view for radial setup with lens and distTargets = 10 mm



Figure 5.16. Front view for radial setup without lens and distTargets = 24 mm

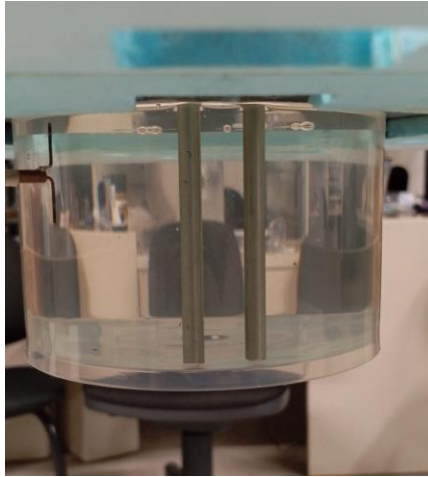


Figure 5.17. Front view for radial setup without lens and distTargets = 14 mm



Figure 5.18. Front view for radial setup without lens and distTargets = 4 mm

As seen in the figures above, the targets were positioned to be upright and parallel. This was done to ensure that, during the antenna's sweeping motion, there would be no interference from the targets in a lower plane. The goal was to minimize reflections from other planes by conducting the sweep solely in one plane.

For comparison, images were generated without the lens, using the setups shown in Figure 5.16, Figure 5.17 and Figure 5.18, to determine whether detection could be achieved without the lens. These results are presented in the figures below:

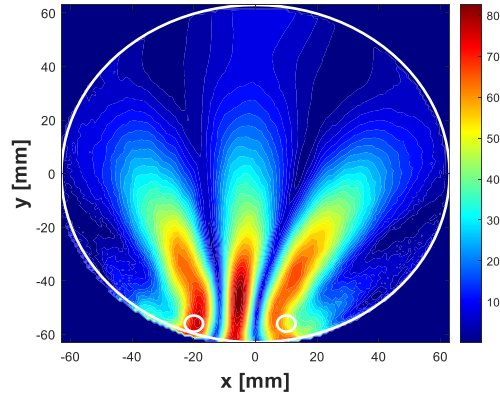


Figure 5.19. Reconstructed image for setup with no lens, with distTarget = 24 mm

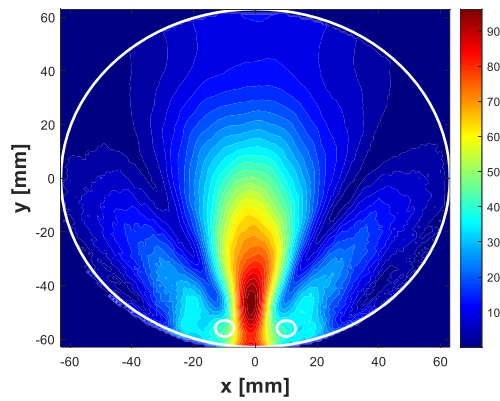


Figure 5.20. Reconstructed image for setup with no lens, with distTarget = 14 mm

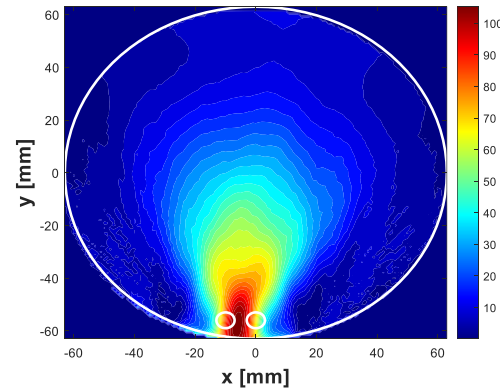


Figure 5.21. Reconstructed image for setup with no lens, with distTarget = 4 mm

From the images obtained without a lens above, it can be concluded that there is detection in the first scenario, as expected, given that the distance between the targets is greater than $\lambda/2$. However, as the targets move closer together, with 14 mm between them (which is less than $\lambda/2$ within the breast), there is only a combined response of the two targets, leading to no detection. The same can be concluded when the targets are 4 mm apart.

Using the image reconstruction algorithm, similar to that performed in the simulations from Chapter 4, which considers an index of refraction in the x direction different from the index of

refraction in the z direction (anisotropic refraction index), and employing the algorithm to minimize the difference between the actual position of the targets and the detected position, the following results were obtained and are presented in the figures below:

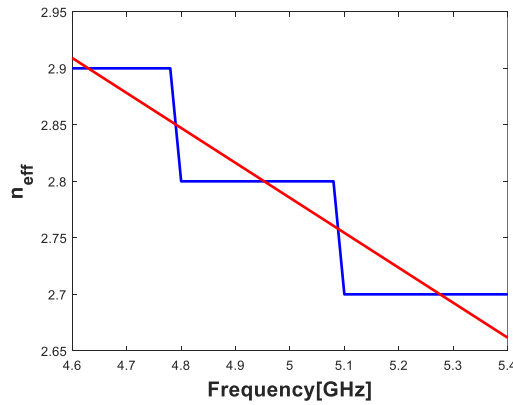


Figure 5.22. Variation of n_x with frequency for slab thickness of 1 mm and cylindrical breast, for the experimental setup

Similarly to the simulations, when the water lens was present, the refractive index will decrease with frequency, as determined by the refractive index selection algorithm described in Chapter 4. Compared to refractive index in the x-direction from the simulation, this experimental n_x is lower. This is because the permittivity of the agar lens is not exactly equal to the permittivity of the water lens, as indicated by the graphs in Figure 5.1, Figure 5.2 and Figure 5.3. A curve fitting was once again performed (shown by the red curve) for this refractive index, and images were generated for these refractive indices, as depicted in the figures below:

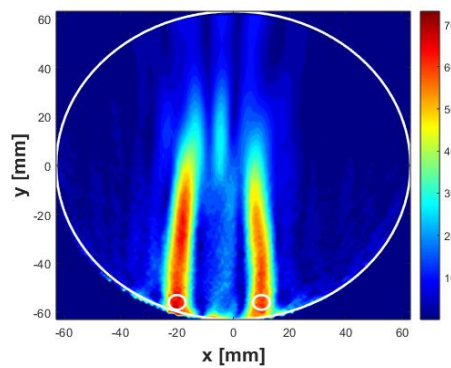


Figure 5.23. Reconstructed image for setup with lens, with distTargets = 24 mm, depth = 0 mm

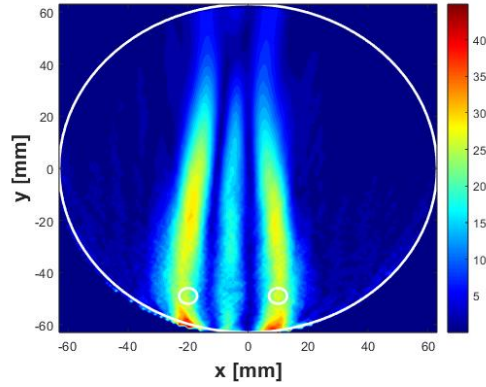


Figure 5.24. Reconstructed image for setup with lens, with $\text{distTargets} = 24 \text{ mm}$, $\text{depth} = 7 \text{ mm}$

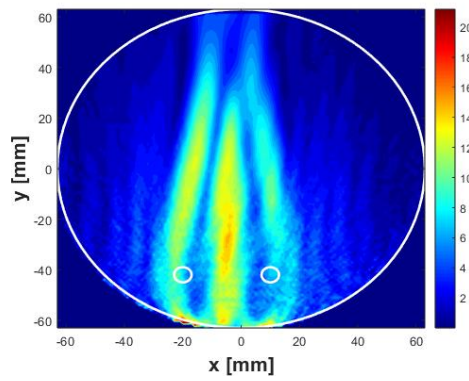


Figure 5.25. Reconstructed image for setup with lens, with $\text{distTargets} = 24 \text{ mm}$, $\text{depth} = 14 \text{ mm}$

As evident from the above figures, where images for various depths are compared, detection is achievable in 2 out of the 3 scenarios (at depths of 0 mm and 7 mm), where the response of the targets is attenuated to approximately half at a depth of 7 mm. Detection was expected as it had already been achieved without the lens.

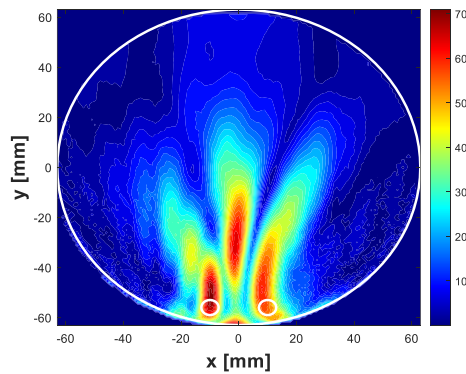


Figure 5.26. Reconstructed image for setup with lens, with $\text{distTargets} = 14 \text{ mm}$, $\text{depth} = 0 \text{ mm}$

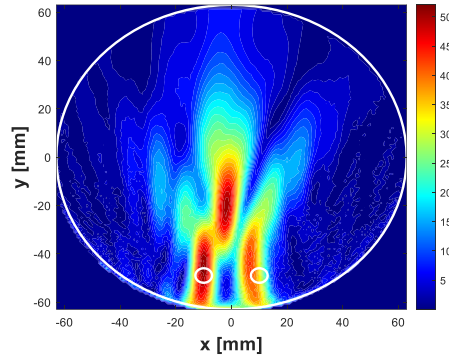


Figure 5.27. Reconstructed image for setup with lens, with $\text{distTargets} = 14$ mm, $\text{depth} = 7$ mm

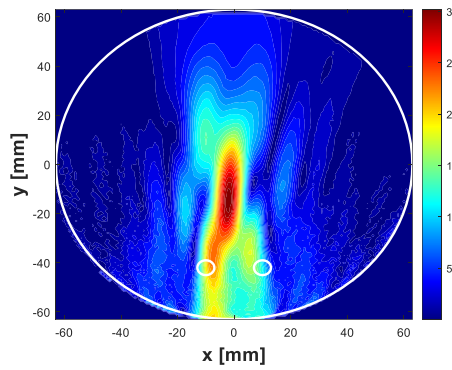


Figure 5.28. Reconstructed image for setup with lens, with $\text{distTargets} = 14$ mm, $\text{depth} = 14$ mm

In this case, where the targets are closer, maintaining a distance between centers of 20 mm (equivalent to $\text{distTargets} = 14$ mm), detection is observed when the targets are at a depth of 0 mm and at a depth of 7 mm. This did not occur in the results without the lens (due to the system being limited by Rayleigh's diffraction). These figures show clear evidence of super-resolution with the use of the agar lens within a medium with electromagnetic properties similar to those of the breast. In Figure 5.28, it is evident that the attenuation is already too high, making it impossible to distinguish the targets, resulting in a combined response rather than separate responses from both targets.

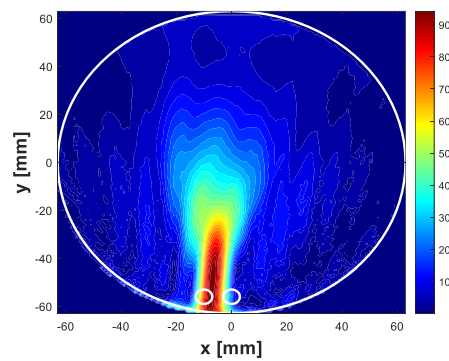


Figure 5.29. Reconstructed image for setup with lens, with $\text{distTarget} = 4$ mm, $\text{depth} = 0$ mm

In this last case, it was not possible to achieve detection, resulting in a clear image showing the sum of the responses from the two targets in the center. This outcome indicates that for a target separation distance of 4 mm, it is not feasible to achieve detection using the agar lens employed. No other depths were tested, as detection was not obtained at a depth of 0 mm.

6 Conclusions

The conclusions chapter aims to summarize the main findings and contributions of this work, as well as to discuss the limitations of the simulations and experimental setups.

6.1 Main achievements

This research explores the use of high-permittivity materials to enhance microwave imaging for breast cancer detection. Its significance lies in revealing the potential of these materials, such as agar and ultrasound gel, to amplify imaging resolution, offering promise for more effective diagnostic techniques in breast cancer detection.

Through this research, the fundamental mechanism of electromagnetic wave propagation in dielectric slabs has been studied, both in symmetric cases (where targets are in free space) and asymmetric cases (where targets are embedded in a medium with a different permittivity than air). Numerical methods and simulations were employed to verify this study, aiming to obtain confirmatory results. The primary challenges in this research lie in finding a balance between frequency and the dielectric slab's thickness (lens) to minimize attenuation and maximize detection. However, achieving this balance is complex because, while increased frequency enhances detection, it also drastically raises attenuation within the breast, resulting in insufficient signal for target detection (tumors).

The main objective of the work was to achieve superior resolution within the breast compared to the resolution obtained by the existing state-of-the-art microwave imaging mechanisms, which do not utilize these super-resolution techniques for better detection. This objective was met, both through simulations and experimental validation. In simulations, an approximate resolution of $\lambda/3$ was obtained for the maximum frequency used, with PE of approximately 3 mm, potentially due to the consideration of a Cartesian geometry in the image reconstruction algorithm and an approximation of the refractive index through frequency using the developed n_x selection algorithm. Experimentally, the achieved resolution was greater than $\lambda/2$ for the maximum frequency used, with PE of approximately 0, as the targets' detection was practically in their actual positions. These results demonstrate that a super lens can enhance breast cancer detection in a way that would not be feasible with a conventional setup without utilizing materials of very high permittivity.

The novelty of the thesis lies in the enhancement of breast cancer detection through the application of super-lenses in microwave imaging. Unlike existing state-of-the-art mechanisms, the study utilizes high-permittivity existing materials, such as agar and ultrasound gel, as lenses to improve resolution and detection capabilities. This innovative approach enables the attainment of superior resolution within the breast area compared to conventional microwave imaging, offering better detection and potentially overcoming the limitations of current imaging technologies.

6.2 Future Work

The research work has made substantial progress in the realm of breast cancer detection through the application of super-resolution microwave imaging. However, numerous areas remain open for further advancements and development.

Primarily, there's an opportunity to refine the choice and composition of materials used as lenses. A deeper exploration and potential refinement of high-permittivity substances might significantly enhance imaging resolution while simultaneously reducing attenuation within breast tissue. In addition, further research on more sophisticated algorithms for image reconstruction could contribute to refining resolution and minimizing positional errors. Investigating non-cartesian geometries or developing more precise methods to determine the refractive index in relation to frequency variations could potentially optimize the imaging process.

Extensive simulations and an in-depth analysis of various configurations and materials could provide valuable insights into the development of a more robust and adaptable approach to breast cancer detection.

Given that this study conducted an overall super-resolution analysis before examining tumor detection in a material simulating the breast, it is feasible to extend this concept to any application featuring a similar geometry. This applies when the detection occurs through the dielectric contrast between materials, whether the material embedding the targets has a permittivity equal to that of air or not.

Bibliography

- [1] “Breast cancer.” Accessed: Oct. 16, 2022. [Online]. Available: <https://www.who.int/news-room/fact-sheets/detail/breast-cancer>
- [2] “Chest X-Ray.” Accessed: Oct. 28, 2023. [Online]. Available: <https://www.breastcancer.org/screening-testing/chest-x-ray>
- [3] “Mammogram X-ray.” Accessed: Oct. 28, 2023. [Online]. Available: <https://www.breastcancer.org/screening-testing/mammograms>
- [4] “Magnetic Resonance Imaging.” Accessed: Oct. 28, 2023. [Online]. Available: <https://www.breastcancer.org/screening-testing/breast-mri>
- [5] “PET scan.” Accessed: Oct. 28, 2023. [Online]. Available: <https://www.breastcancer.org/screening-testing/pet-scans>
- [6] N. K. Nikolova, “Microwave imaging for breast cancer,” *IEEE Microw Mag*, vol. 12, no. 7, pp. 78–94, Dec. 2011, doi: 10.1109/MMM.2011.942702.
- [7] R. A. Martins, J. M. Felicio, J. R. Costa, and C. A. Fernandes, “Systematic Analysis of Microwave Breast Imaging Detection of Different-Sized Malignant and Benign Tumors; Systematic Analysis of Microwave Breast Imaging Detection of Different-Sized Malignant and Benign Tumors,” 2022.
- [8] J. M. Felicio, J. M. Biucas-Dias, J. R. Costa, and C. A. Fernandes, “Microwave Breast Imaging Using a Dry Setup,” *IEEE Trans Comput Imaging*, vol. 6, pp. 167–180, 2020, doi: 10.1109/TCI.2019.2931079.
- [9] “Lecture 17 Dielectric Slab Waveguides.” Accessed: Oct. 30, 2023. [Online]. Available: <https://engineering.purdue.edu/wcchew/ece604s21/Lecture%20Notes/Lect17.pdf>
- [10] M. G. Silveirinha, C. A. Fernandes, and J. R. Costa, “Superlens made of a metamaterial with extreme effective parameters,” *Phys Rev B Condens Matter Mater Phys*, vol. 78, no. 19, Nov. 2008, doi: 10.1103/PhysRevB.78.195121.
- [11] “slab_waveguide”, Accessed: Oct. 30, 2023. [Online]. Available: http://pongsak.ee.engr.tu.ac.th/le426/doc/slab_waveguide.pdf
- [12] “Ajmal Thesis Chapter 2.” Accessed: Oct. 30, 2023. [Online]. Available: https://faculty.kfupm.edu.sa/ee/ajmal/files/Ajmal_Thesis_Chap2.pdf
- [13] Q. Yao and W. Qifu, “Kirchoff Migration Algorithm for Ground Penetrating Radar Data,” in *2012 International Conference on Computer Science and Electronics Engineering*, IEEE, Mar. 2012, pp. 396–398. doi: 10.1109/ICCSEE.2012.256.

- [14] K. Santos, C. Fernandes, and J. Costa, "Microwave Imaging Using the Kirchhoff Migration Algorithm with Monostatic Configuration," in *Anais de XXXIV Simpósio Brasileiro de Telecomunicações*, Sociedade Brasileira de Telecomunicações, 2016. doi: 10.14209/sbrt.2016.18.
- [15] J. M. Felício, J. M. Bioucas-Dias, J. R. Costa, and C. A. Fernandes, "Antenna Design and Near-Field Characterization for Medical Microwave Imaging Applications," *IEEE Trans Antennas Propag*, vol. 67, no. 7, pp. 4811–4824, Jul. 2019, doi: 10.1109/TAP.2019.2905742.
- [16] M. Tabib-Azar, J. L. Katz, and LeClair, "Evanescent microwaves: a novel super-resolution noncontact nondestructive imaging technique for biological applications," *IEEE Trans Instrum Meas*, vol. 48, no. 6, pp. 1111–1116, 1999, doi: 10.1109/19.816123.
- [17] M. G. Silveirinha, C. R. Medeiros, C. A. Fernandes, and J. R. Costa, "Experimental verification of broadband superlensing using a metamaterial with an extreme index of refraction," *Phys Rev B Condens Matter Mater Phys*, vol. 81, no. 3, Jan. 2010, doi: 10.1103/PhysRevB.81.033101.
- [18] Y. Kondo, X.-H. Han, and Y.-W. Chen, "Two-step learning based super resolution and its application to 3D medical volumes," in *2015 IEEE 4th Global Conference on Consumer Electronics (GCCE)*, IEEE, Oct. 2015, pp. 326–327. doi: 10.1109/GCCE.2015.7398738.
- [19] L.-Y. Xiao, R. Hong, L.-Y. Zhao, H.-J. Hu, and Q. H. Liu, "A Hybrid Neural Network Electromagnetic Inversion Scheme (HNNEMIS) for Super-Resolution 3-D Microwave Human Brain Imaging," *IEEE Trans Antennas Propag*, vol. 70, no. 8, pp. 6277–6286, Aug. 2022, doi: 10.1109/TAP.2022.3146571.
- [20] P. Shah and M. Moghaddam, "Super resolution for microwave imaging: A deep learning approach," in *2017 IEEE International Symposium on Antennas and Propagation & USNC/URSI National Radio Science Meeting*, IEEE, Jul. 2017, pp. 849–850. doi: 10.1109/APUSNCURSINRSM.2017.8072467.
- [21] L. Y. Zhao, L. Y. Xiao, Y. Cheng, R. Hong, and Q. H. Liu, "Machine-Learning-Based Inversion Scheme for Super-Resolution Three-Dimensional Microwave Human Brain Imaging," *IEEE Antennas Wirel Propag Lett*, vol. 21, no. 12, pp. 2437–2441, Dec. 2022, doi: 10.1109/LAWP.2022.3196189.
- [22] M. S. Greeshma and V. R. Bindu, "Super-resolution using Deep Networks for Chest X-Ray Images," in *Proceedings of the IEEE International Conference Image Information Processing*, Institute of Electrical and Electronics Engineers Inc., 2021, pp. 198–201. doi: 10.1109/ICIIP53038.2021.9702582.

- [23] J. Christensen and F. J. García De Abajo, "Slow plasmonic slab waveguide as a superlens for visible light," *Phys Rev B Condens Matter Mater Phys*, vol. 82, no. 16, Oct. 2010, doi: 10.1103/PhysRevB.82.161103.
- [24] R. Dhama, B. Yan, C. Palego, and Z. Wang, "Super-resolution imaging by dielectric superlenses: Tio2 metamaterial superlens versus batio3 superlens," *Photonics*, vol. 8, no. 6, Jun. 2021, doi: 10.3390/photonics8060222.
- [25] P. Meng, S. F. Pereira, X. Dou, and H. P. Urbach, "Superresolution effect due to a thin dielectric slab for imaging with radially polarized light," *Opt Express*, vol. 28, no. 14, p. 20660, Jul. 2020, doi: 10.1364/oe.390602.
- [26] N. Waterman, I. Styles, S. Thomas, and S. Zhang, "Super-resolution Imaging with Metamaterials for Cardiovascular Disease," in *Optics in the Life Sciences*, Optica Publishing Group, 2015, p. JT3A.10. [Online]. Available: <https://opg.optica.org/abstract.cfm?URI=NTM-2015-JT3A.10>
- [27] M. G. Silveirinha, C. R. Medeiros, C. A. Fernandes, and J. R. Costa, "Resolving subwavelength objects with a crossed wire mesh superlens operated in backscattering mode," *New J Phys*, vol. 13, May 2011, doi: 10.1088/1367-2630/13/5/053004.
- [28] "CST Microwave Studio™ 2021." [Online]. Available: www.cst.com
- [29] The MathWorks Inc., "MATLAB®2019." [Online]. Available: <https://www.mathworks.com/products/matlab.html>
- [30] J. de S. Marinho, K. Santos, and E. F. da Silva, "Caracterização de Phantoms usando Sonda Coaxial para Aplicações Biomédicas," in *Anais do XXXIX Simpósio Brasileiro de Telecomunicações e Processamento de Sinais*, Sociedade Brasileira de Telecomunicações, 2021. doi: 10.14209/sbrt.2021.1570731660.
- [31] N. Joachimowicz, C. Conessa, T. Henriksson, and B. Duchêne, "Breast phantoms for microwave imaging," *IEEE Antennas Wirel Propag Lett*, vol. 13, pp. 1333–1336, 2014, doi: 10.1109/LAWP.2014.2336373.